

# Stability of a vortex in radial density stratification: role of wave interactions

HARISH N. DIXIT<sup>†</sup> AND RAMA GOVINDARAJAN<sup>‡</sup>

Engineering Mechanics Unit, Jawaharlal Nehru Centre for Advanced Scientific Research,  
Bangalore 560064, India

(Received 3 September 2010; revised 18 March 2011; accepted 26 March 2011;  
first published online 25 May 2011)

We study the stability of a vortex in an axisymmetric density distribution. It is shown that a light-cored vortex can be unstable in spite of the ‘stable stratification’ of density. Using a model flow consisting of step jumps in vorticity and density, we show that a wave interaction mediated by shear is the mechanism for the instability. The requirement is for the density gradient to be placed outside the vortex core but within the critical radius of the Kelvin mode. Conversely, a heavy-cored vortex, found in other studies to be unstable in the centrifugal Rayleigh–Taylor sense, is stabilized when the density jump is placed in this region. Asymptotic solutions at small Atwood number  $At$  show growth rates scaling as  $At^{1/3}$  close to the critical radius, and  $At^{1/2}$  further away. By considering a family of vorticity and density profiles of progressively increasing smoothness, going from a step to a Gaussian, it is shown that sharp gradients are necessary for the instability of the light-cored vortex, consistent with recent work which found Gaussian profiles to be stable. For sharp gradients, it is argued that wave interaction can be supported due to the presence of *quasi-modes*. Probably for the first time, a quasi-mode which decays exponentially is shown to interact with a neutral wave to give exponential growth in the combined case. We finally study the nonlinear stages using viscous direct numerical simulations. The initial exponential instability of light-cored vortices is arrested due to a restoring centrifugal buoyancy force, leading to stable non-axisymmetric structures, such as a tripolar state for an azimuthal wavenumber of 2. The study is restricted to two dimensions, and neglects gravity.

**Key words:** internal waves, vortex instability, waves in rotating fluids

---

## 1. Introduction

Density variation in the neighbourhood of vortices occurs in many natural systems and technological applications. Large-scale geophysical vortices can be subjected to strong density variations, often along their axis, and occasionally perpendicular to it. The latter configuration, especially in the form of an axisymmetric flow with radial density variations, has been the subject of numerous papers, and is under study here. The primary focus has been on the destabilization of heavy-cored vortices. Such a vortex, where the density is a monotonically decreasing function of radius, is expected to undergo a centrifugal Rayleigh–Taylor instability (CRTI). In the present work, we

<sup>†</sup> Present address: Department of Mathematics, University of British Columbia, Vancouver, Canada.

<sup>‡</sup> Email address for correspondence: rama@jncasr.ac.in

show that a light-cored vortex may become unstable for certain configurations, while a heavy-cored one may be stabilized.

The CRTI is the circular analogue of the classical Rayleigh–Taylor instability (RTI) with gravity replaced by the centrifugal acceleration. However, while the RTI can exist without a mean flow, centrifugal forces are generated due to the vortex, and this makes the analogy incomplete. A more direct theoretical analog of the planar RTI is a radial density variation in a flow which is entirely in solid-body rotation, where shear is absent. Such a configuration was investigated by Fung & Kurzweg (1975) with an algebraically varying density. They also study the 3D stability of a radially stratified Rankine-type vortex, but the density jump was fixed at the edge of the core. This work was a generalization of the earlier study of Uberoi, Chow & Narain (1972) on the stability of a Rankine vortex. In a later work, Fung (1983) studied the stability of a three-layer rotating fluid, each region with a fixed angular velocity and density. This is analogous to the planar three-layer fluid first considered by Taylor (1931). In geophysical flows, there is an interest in understanding the baroclinic instability process, discussed in detail in Vallis (2006). It was shown by Saunders (1973) experimentally that radial density variation in a baroclinic vortex drives a CRTI. Nadiga & Aurnou (2008) came up with an excellent expository article on the phenomenon. For an idealized compressible fluid rotating in a pipe, Gans (1975) considered density variations in the radial direction, and noted that the stability depends on a ‘centrifugal Richardson number’.

In all the above studies, shear does not play a role. We shall see below how the presence of shear in a vortical flow can have important implications for the stability of the system. In particular, it will be shown that shear can cause the destabilization of a light-cored vortex, or stabilize a heavy-cored vortex. The latter situation finds some mention in Joly, Fontane & Chassaing (2005), but the former has not been seen before, to our knowledge. In parallel flows, various combinations of density stratification and shear have been well investigated. As an extension of the popular semi-circle theorem of Howard (1961), a semi-ellipse criterion for plane stratified flows was derived by Kochar & Jain (1979) to define the possible range of phase speeds. This theorem was shown to hold for the cylindrical case as well by Fung (1983), and applies to the present flow of a vortex with radial density stratification.

Kurzweg (1969) was one of the earliest to consider non-axisymmetric disturbances, and derived a sufficient condition for stability for a smooth vortex with radial density variation. Necessary conditions for the stability of the same flow were given by Eckhoff & Storesletten (1978, 1980). To the best of our knowledge, there is no necessary and sufficient condition for *instability* of a vortex subject to radial density stratification. A summary of various necessary and sufficient conditions for stability/instability of this flow is given by Sipp *et al.* (2005). The stability of a heavy-cored Gaussian vortex with a Gaussian density distribution was studied by Sipp *et al.* (2005) and Joly *et al.* (2005). These studies are complementary to each other. While the former shows that a competition between 3D centrifugal instabilities and 2D Rayleigh–Taylor instabilities can occur, the latter restricts their analysis to two dimensions and includes the nonlinear stages of RTI. Here, in agreement with Coquart, Sipp & Jacquin (2005), they show that wave-like motions on the vortex core amplify and result in the breakdown of the vortex into multiple parts, reminiscent of the breakdown of a baroclinic vortex observed by Saunders (1973). The number of parts is governed by the wavenumber of the linear perturbation. These workers found that CRTI is stabilized for density core sizes comparable to the vortex core, and realized that shear has a role to play in the stabilization. Incidentally, a similar

mechanism was predicted by Lees (1958) in boundary-layer flow over a convex surface.

Importantly, Joly *et al.* (2005) noted that a light-cored Gaussian vortex, where density increases monotonically away from the vortex centre, is always stable. Our work confirms their result for a Gaussian vortex, but we show that the smoothness of the vortex profile plays a crucial role, so a light-cored vortex is not always stable. This result may appear counter-intuitive at first sight, but is shown to be a natural consequence of wave interactions. Using a Rankine vortex and a step density jump located at a given radial location, we explicitly show that the Kelvin wave supported at the edge of the vortex core is allowed, due to shear, to interact with density waves, leading to stabilization/destabilization. For a Gaussian vortex however, shear and vorticity gradient co-exist everywhere, and this clouds the interaction between the two. In our recent work on a more generic density stratification (Dixit & Govindarajan 2010), we obtained one instance of a Rankine vortex surrounded by lighter fluid immediately outside the core, where a configuration which is unstable in terms of density stratification is rendered neutrally stable. A desire to understand this result motivated the present study.

Wave interactions have been observed to cause instability on numerous occasions in the past. Taylor (1931) was among the earliest to observe that 'stable' density stratification can give rise to instabilities in a three-layer planar model. He attributed this to the interaction of waves on two interfaces. A detailed study of the wave interaction mechanism for instabilities is given in Sakai (1989). For a homogeneous shear layer with two vorticity interfaces, Hoskins, McIntyre & Robertson (1985) showed that instability is due to a linear wave interaction of counter-propagating Rossby waves riding at these interfaces. An exhaustive survey of stratified shear flow instabilities with broken-line profiles is given in Howard & Maslowe (1973). But at the time of that survey, a clear kinematic understanding of the instability process in terms of wave interactions did not exist. The wave interaction mechanism was extended to stratified shear flows recently by Baines & Mitsudera (1994) and Harnik *et al.* (2008). We apply this mechanism to a stratified vortex geometry. The phase between the interface displacement and the normal velocity component is an important driver for both stabilization and destabilization, as will be demonstrated below. We further discuss the role of the critical layer.

In the present flow, the interaction is between Kelvin waves riding on the vortex core, and internal waves riding on the density interface. The Kelvin waves are analogous to Rossby waves due to a potential vorticity gradient, and are sometimes referred to by this name (see McWilliams, Graves & Montgomery (2003); Schecter & Montgomery (2003)). We neglect gravity, so the internal waves are caused solely by centrifugal forces. The wave interaction is easy to obtain analytically, as we do, when both vorticity gradient and density profiles are imposed in the form of step functions. We then need to describe what happens with smooth vorticity profiles, which do not support discrete Kelvin waves. We hypothesize that the wave interaction mechanism is now between the quasi-modes from the vorticity field and internal waves from the density field. For this, we follow the work of Briggs, Daugherty & Levy (1970) and of Schecter *et al.* (2000) showing that when a piecewise continuous profile is smoothed, discrete modes are replaced by quasi-modes, which are a collective response of the continuous spectrum modes. A detailed mathematical treatment of quasi-modes in boundary layer flows is available in Shrira & Sazonov (2001), along with a discussion on the usage of piecewise linear approximations in stability theory.

The present work is the first to our knowledge where a quasi-mode, which is exponentially decaying, and a neutral discrete mode are shown to interact to give exponential growth. However, there have been some studies which have investigated the interaction between continuous spectrum modes and discrete modes. Voronovich, Pelinovsky & Shrira (1998*a*) and Voronovich, Shrira & Stepanyants (1998*b*) study the interaction of boundary-layer quasi-modes with internal gravity waves in the ocean. Similarly Voronovich & Rybak (1978) and Romanova & Shrira (1988) study the interaction of boundary-layer quasi-modes with gravity-capillary waves at an air/water interface. Sazonov (1989) showed that the resonant interaction between discrete spectrum and continuous spectrum modes leads to a linear growth of disturbances in time, and provided a physical interpretation of this algebraic instability. Vanneste (1996) also considered an interaction between discrete (regular) and continuous (singular) spectrum modes, and clarified that when dealing with continuous spectrum interaction, one needs to consider a packet of these modes together. As a result, the contribution of continuous spectrum modes appears in terms of integrals over the physical domain, with quasi-modes being a special case.

The paper is organized as follows. The problem is formulated in §2. Base flow profiles and the governing equations are discussed here. The case of a Rankine vortex with step density jump is considered in §3, and the mechanism is elaborated for light-cored vortices. We then extend the stability of light-cored vortices to smooth profiles in §4. Landau poles for various vorticity profiles are extracted, and their connection to quasi-modes is discussed. A linear initial value problem is solved numerically for comparison. Results from direct numerical simulations for light-cored vortices are presented in §5 and concluding remarks are provided in §6.

## 2. Formulation

We consider the range of vorticity profiles from a Rankine to a Gaussian vortex. The density jump may also be step-like or smooth, and can be located at any radial location.

### 2.1. Base flow profiles

We define a family of vorticity profiles with the same circulation as that of a Gaussian vortex of core size  $a$ . The vorticity profile depends on a single parameter  $n$  in the following way:

$$Z = Z_0 \exp \left[ - \left( \frac{r}{\delta_z} \right)^{2n} \right], \quad (2.1)$$

where  $Z_0$  is the vorticity at the vortex centre, and  $\delta_z$  is the vortex core size. The total circulation is given by

$$\mathcal{E} \equiv 2\pi \int_0^\infty Z(r)r \, dr = \frac{\pi Z_0 \delta_z^2}{n} \Gamma(1/n), \quad (2.2)$$

where  $\Gamma(\cdot)$  is the gamma function. When  $n = 1$ , the vorticity profile simplifies to a simple Gaussian form. For a Gaussian vortex of core size  $a$ , the circulation is equal to  $\pi Z_0 a^2$ . To keep the circulation fixed at this value for all  $n$ , we define the core size  $\delta_z$  as

$$\delta_z = a \left[ \frac{n}{\Gamma(1/n)} \right]^{1/2}. \quad (2.3)$$

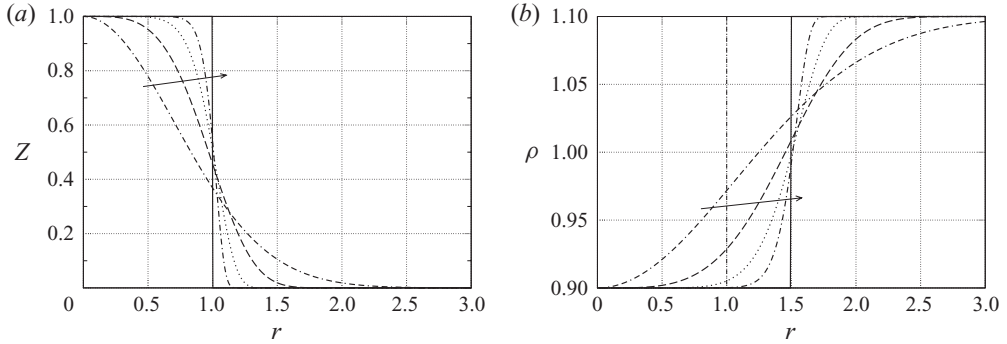


FIGURE 1. (a) Vorticity and (b) density profiles as functions of  $n$ . From left to right (indicated by arrow),  $n = 1, 2, 4, 8, \infty$  going from a Gaussian to a step profile. In this representative figure, the core sizes for vorticity and density are chosen as  $a = 1$  and  $r_j = 1.5$ , respectively, and the Atwood number  $At = 0.1$ .

At  $n = 1$ , we obtain a Gaussian profile, and as  $n \rightarrow \infty$ , the profiles assume a step-like shape as shown in figure 1. While we keep the numerical values of  $Z_0$  and  $a$  fixed at 1 for simplicity, we retain these variables in the algebra for generality. The effect of smoothness can also be studied by imposing hyperbolic tangent profiles of varying width (see, e.g. Hall, Bassom & Gilbert (2003)), but the present family was chosen for two reasons. The Gaussian profile at  $n = 1$  makes for straightforward comparison with earlier work, and it is easier in (2.1) rather than with a tanh to enforce the same circulation for each profile. We believe our conclusions are valid for all types of smooth profiles. Since the vorticity for any  $n$  is monotonically decreasing, i.e.

$$\frac{dZ}{dr} < 0, \tag{2.4}$$

for all  $r$ , discrete vorticity (Kelvin) modes do not exist (see Briggs *et al.* (1970)) except when  $n = \infty$ . In this limit, we get a Rankine vortex, which supports a single discrete mode due to a vorticity discontinuity at  $r = a$ . An artefact of the family of profiles thus constructed is a small variation of the core size with  $n$ . From (2.3) we find that the core size  $\delta_z$  is equal to unity for Rankine and Gaussian profiles, but is slightly higher for intermediate profiles, with a maximum of about 1.06 at  $n \approx 2.17$ .

Unless otherwise specified, density profiles are defined analogous to vorticity profiles as

$$\bar{\rho} = \rho_2 + (\rho_1 - \rho_2) \exp \left[ - \left( \frac{r}{\delta_\rho} \right)^{2n} \right], \tag{2.5}$$

where  $\delta_\rho$  is the density core size,  $\rho_1$  is the density near the vortex centre and  $\rho_2$  is the far-field value. We further define the location of the density interface,  $r_j$ , as

$$r_j = \frac{\delta_\rho}{\delta_z} a. \tag{2.6}$$

When  $r_j > a$ , the density core is larger than the vortex core. Another artefact of these profiles is that the density gradient varies with  $n$  and  $r_j$ . Varying the location of the density jump affects the gradient value, and this becomes severe for large  $n$ . To overcome this difficulty, and more importantly, to estimate the effect of smoothing the vorticity profile alone, we make use of tanh density profiles in the stability analysis

of §4, defined by

$$\bar{\rho} = \frac{1}{2} \left[ (\rho_1 + \rho_2) - (\rho_1 - \rho_2) \tanh \left( \frac{r - r_j}{\delta_r} \right) \right]. \tag{2.7}$$

For these profiles, steepness does not depend on  $r_j$  but is controlled by the factor  $\delta_r$ , fixed here at a value of 0.1.

2.2. Governing equations

The appropriate governing equations are the two-dimensional Navier–Stokes equations in  $r - \theta$  coordinates. A small-amplitude perturbation  $(u'_r, u'_\theta, \rho')$  is imposed on the axisymmetric base vorticity and density profiles. Using a Fourier decomposition in the azimuthal direction, i.e.

$$[u'_r, u'_\theta, \rho'](r, \theta, t) = \text{Re}\{[\tilde{u}_r, \tilde{u}_\theta, \tilde{\rho}](r, t) \exp[i m \theta]\}, \tag{2.8}$$

the linearized system of equations for  $\tilde{\mathbf{y}} = [\tilde{u}_r, \tilde{\rho}]$  can be written in the form

$$\frac{\partial}{\partial t} (\mathbf{M} \tilde{\mathbf{y}}) = -i \mathbf{N} \tilde{\mathbf{y}}, \tag{2.9}$$

where the operators are given by

$$\mathbf{M} = \begin{bmatrix} \bar{\rho} \mathbf{L} + (\mathcal{D} \bar{\rho}) r^2 \mathcal{D}^* & 0 \\ 0 & 1 \end{bmatrix}, \tag{2.10}$$

$$\mathbf{N} = \begin{bmatrix} \bar{\rho} m (\Omega \mathbf{L} - r \mathcal{D} \mathbf{Z}) + (\mathcal{D} \bar{\rho}) m (\Omega r^2 \mathcal{D}^* - r \mathbf{Z}) & -i m^2 r \Omega^2 \\ -i \mathcal{D} \bar{\rho} & m \Omega \end{bmatrix}, \tag{2.11}$$

$$\mathbf{L} = r^2 \mathcal{D}^2 + 3r \mathcal{D} - (m^2 - 1). \tag{2.12}$$

Here  $\mathcal{D} = d/dr$  and  $\mathcal{D}^* = \mathcal{D} + 1/r$ . The azimuthal velocity component  $\tilde{u}_\theta$  can be computed from  $\tilde{u}_r$  using the continuity equation. The base state angular velocity  $\Omega(r)$  is given by

$$\Omega(r) = \frac{Z_0 \delta_z^2}{2nr^2} \Gamma \left[ \left( \frac{r}{\delta_z} \right)^{2n}, 1/n \right] \Gamma(1/n), \tag{2.13}$$

where  $\Gamma(\cdot, \cdot)$  is the incomplete gamma function (see, e.g. Abramowitz & Stegun 1972). The boundary conditions are that perturbations decay to zero at the vortex axis and as  $r \rightarrow \infty$ . The perturbation vorticity  $\zeta(r, t)$  is related to  $\tilde{u}_r$  and  $\tilde{u}_\theta$  as

$$\zeta(r, t) = \frac{1}{r} \frac{\partial(r \tilde{u}_\theta)}{\partial r} - \frac{i m}{r} \tilde{u}_r. \tag{2.14}$$

For a normal mode in time

$$[\tilde{u}_r(r, t), \tilde{u}_\theta(r, t), \tilde{\rho}(r, t)] = [u_r(r), u_\theta(r), \rho(r)] \exp[-i \omega t], \tag{2.15}$$

and a single equation in  $u_r$  can be written as

$$\mathcal{D}(\bar{\rho} r^2 \mathcal{D}^* u_r) + \left[ \frac{m^2 r \Omega^2 \mathcal{D} \bar{\rho}}{(\omega - m \Omega)^2} + \frac{m r \mathcal{D}(\bar{\rho} \mathcal{D}^*(r \Omega))}{(\omega - m \Omega)} - m^2 \bar{\rho} \right] u_r = 0. \tag{2.16}$$

This equation is analogous to the Taylor-Goldstein equation for planar flow (Drazin & Reid 1981), and has been derived earlier by Fung & Kurzweg (1975) and others. The boundary conditions are  $u_r = 0$ , at  $r = 0$  for  $m \geq 2$ , and at  $r \rightarrow \infty$ . We will consider

only wavenumbers  $m \geq 2$  as  $m = 1$  is only a translational mode in 2D, and does not alter the dynamics. The centrifugal acceleration  $r\Omega^2$  in the first term in the bracket is analogous to gravity in a planar flow. Thus, unlike in the planar situation, internal waves supported by density inhomogeneity do not have an existence independent of the flow. When  $\omega$  is real, the flow is always neutrally stable, and when the imaginary part of  $\omega$  is positive, the flow is unstable.

### 3. Stability of a Rankine vortex with density jump

The limit  $n \rightarrow \infty$  corresponding to a Rankine vortex with a step density jump allows for analytical solutions, and is therefore considered in some detail. We keep the location of the density jump arbitrary. When the vorticity is constant everywhere, i.e. the entire flow is in solid-body rotation, Fung (1983) showed that no instability can occur when  $D\bar{\rho} > 0$ , which is an intuitive result. We repeat this proof for clarity. Substituting  $\Omega(r) = \Omega_0$ ,  $c = \omega/m$  and  $u_r = \Psi/r$  in (2.16), we get

$$\mathcal{D}(\bar{\rho}r\mathcal{D}\Psi) + \left[ \frac{-m^2\bar{\rho}}{r} + \Lambda\mathcal{D}\bar{\rho} \right] \Psi = 0, \quad (3.1)$$

where

$$\Lambda = \frac{\Omega_0^2}{(c - \Omega_0)^2} + \frac{2\Omega_0}{(c - \Omega_0)}. \quad (3.2)$$

Equation (3.1) along with homogeneous boundary conditions at  $r = 0$  and  $\infty$  is in a Sturm–Liouville or self-adjoint form, so  $\Lambda$  is purely real, with the same sign as  $\mathcal{D}\bar{\rho}$ . Rewriting (3.2) as

$$c = \Omega_0 \left[ \frac{(1 + \Lambda) \pm \sqrt{1 + \Lambda}}{\Lambda} \right], \quad (3.3)$$

we see that a density jump from light to heavy is always stable, since  $\Lambda$  is now positive and so  $c$  has only real solutions. Note, however, that the reverse case of a heavy core is not unstable unless  $\Lambda < -1$ .

On the other hand, for the irrotational flow near a point vortex, where angular velocity varies as  $\Omega = \Gamma/r^2$ , we get

$$\Lambda = \frac{1}{(c - \Omega)^2}. \quad (3.4)$$

Again, we arrive at the result that there is no instability when  $\mathcal{D}\bar{\rho} > 0$ , but when  $\mathcal{D}\bar{\rho} < 0$ , there is always an instability. In our flow, a density jump placed at  $r \ll a$  or  $r \gg a$ , respectively, resembles the limits of solid-body rotation or a point vortex. A positive density jump being stable in either of these limits, one may expect a light-cored vortical flow to be stable wherever the jump is placed. This will be shown below to be not true. The reason is that while (2.16) can be reduced to (3.1) either inside or outside the vortex core, it still is not a Sturm–Liouville system as homogeneous boundary conditions are not satisfied at  $r = a$ , a region of non-zero vorticity gradient. There is thus an opportunity for different behaviour if the jump is placed at  $r \sim a$ . Note also that this system is not self-adjoint.

The  $n \rightarrow \infty$  limit may be described as

$r \leq a$	$a < r \leq r_j$	$r > r_j$	
$Z = Z_0$	$Z = 0$	$Z = 0$	(3.5)
$\Omega = \Omega_0$	$\Omega = \Omega_0 a^2 / r^2$	$\Omega = \Omega_0 a^2 / r^2$	
$\bar{\rho} = \rho_1$	$\bar{\rho} = \rho_1$	$\bar{\rho} = \rho_2$	

The general solution of (2.16) in the above three regions is in general a linear combination of the solutions  $r^{(m-1)}$  and  $r^{(-m-1)}$ . For  $r \leq a$ , for finiteness of  $u_r$  at the vortex centre, the solution is of the form  $r^{(m-1)}$  and for  $r > r_j$ , for the solution to decay uniformly as  $r \rightarrow \infty$ , the solution is of the form  $r^{-(m+1)}$ , whereas in the intermediate region, the solution involves a linear combination of the above two forms. The coefficients appearing in the above solution are obtained by matching the value of  $u_r$  and pressure at the interfaces  $r = a$  and  $r = r_j$ . In Appendix A, the eigenfunctions  $u_r$  are given along with the necessary steps for the derivation of the dispersion relation. Non-dimensionalizing  $\omega$  by the maximum core vorticity  $Z_0$ , a cubic eigenvalue equation can be obtained from (2.16) as follows:

$$\omega^3 + a_2 \omega^2 + a_1 \omega + a_0 = 0, \tag{3.6}$$

where

$$a_2 = \frac{1}{2} \left( 1 - m \left[ 1 + 2 \left( \frac{a}{r_j} \right)^2 \right] + At \left( \frac{a}{r_j} \right)^{2m} \right), \tag{3.7}$$

$$a_1 = \frac{m}{4} \left( 2(m-1) \left( \frac{a}{r_j} \right)^2 - 2At \left( \frac{a}{r_j} \right)^{2m+2} + (m+At) \left( \frac{a}{r_j} \right)^4 \right), \tag{3.8}$$

$$a_0 = \frac{m(m-1)}{8} \left( At \left( \frac{a}{r_j} \right)^{2m+4} - (m+At) \left( \frac{a}{r_j} \right)^4 \right), \tag{3.9}$$

and  $At = (\rho_1 - \rho_2) / (\rho_1 + \rho_2)$  is the Atwood number. In the homogeneous fluid limit of  $At = 0$ , (3.6) is solved to give a 2D Kelvin mode,  $\omega_0^{(1)}$ , on the vortex core boundary, and a single continuous spectrum mode,  $\omega_0^{(2,3)}$ , at any  $r = r_j$ , given, respectively, by

$$\omega_0^{(1)} = \frac{(m-1)}{2}, \quad \omega_0^{(2,3)} = \frac{ma^2}{2r_j^2}. \tag{3.10}$$

The subscript 0 denotes the case of  $At = 0$ . The discrete mode is obtained due to a non-zero vorticity gradient at  $r = a$ . The continuous spectrum of a Rankine vortex is studied in detail in a forthcoming work of A. Roy and G. Subramanian (private communication). The critical radius for the Kelvin mode is obtained by equating the two solutions of (3.10) giving

$$r_c = a \sqrt{\frac{m}{m-1}}. \tag{3.11}$$

The angular speed of the base flow at this radius is equal to that of the Kelvin mode. In a frame of reference rotating with this speed, disturbance waves rotate in opposite directions on either side of  $r_c$ . The continuous spectrum outside the core can result in interesting behaviour for  $At \neq 0$ . Romanova (2008), for instance, showed that the continuous spectrum modes of a homogeneous flow can become unstable

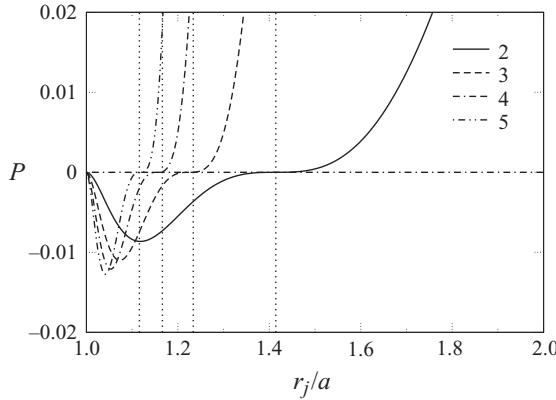


FIGURE 2. Curves of  $\mathcal{P}$  from (3.12) plotted as functions of the density jump location  $r_j/a$ . The wave number  $m$  corresponding to each curve is shown in the legend. In the limit of small  $At$ , the flow is unstable when  $\mathcal{P} > 0$ . The dotted vertical lines indicating the zero crossings of  $\mathcal{P}$  coincide in each case with the critical radius for the Kelvin mode obtained from (3.11).

eigenmodes in the presence of density stratification. We therefore restrict our study to the region  $r_j > a$ .

### 3.1. Heavy-cored Rankine vortex

We first consider  $At > 0$ , which means that fluid within  $r_j$  is heavier than that outside it. Following the standard methods of solving a cubic equation (Press *et al.* 1992), a criterion for instability can be derived. As the general criterion is cumbersome, we give here the small  $At$  approximation, retaining up to  $O(At)$ . For instability, we require

$$\mathcal{P} = \left(1 - m + m \left(\frac{a}{r_j}\right)^2\right)^3 \left(1 - m + m \left(\frac{a}{r_j}\right)^2 - \left(\frac{a}{r_j}\right)^{2m}\right) > 0. \tag{3.12}$$

Figure 2 shows curves of  $\mathcal{P}$  plotted as a function of  $r_j/a$ . The zero crossing occurs when the jump is placed exactly at the critical radius, i.e.  $r_j = r_c$ . As the Atwood number increases, a jump placed anywhere outside  $r_c$  becomes increasingly unstable, and the unstable range encroaches within  $r_c$  as well, but the flow is neutrally stable for a range of  $r_j$  immediately outside the Rankine core. This can be seen in figure 3(a), where the growth rate is plotted as a function of the Atwood number for a fixed wavenumber  $m = 2$ . Figure 3(b) shows that a neutral region exists for all  $m$ . Here, no assumption is made on the smallness of  $At$ .

The complete dispersion relation in the  $At - r_j/a$  plane for  $m = 2$  is plotted in figure 4, where a region of stabilization can clearly be seen for small  $At$  and  $r_j/a$ . For a density jump which coincides with the core, i.e.  $r_j = a$ , (3.6) reduces to the simple form

$$\omega = \frac{m}{2} - \left[ \frac{(1 + At)}{4} \left( 1 \pm \sqrt{1 - \frac{4mAt}{(1 + At)^2}} \right) \right]. \tag{3.13}$$

Therefore, instability occurs at the core only if

$$m > \frac{(1 + At)^2}{4At}. \tag{3.14}$$

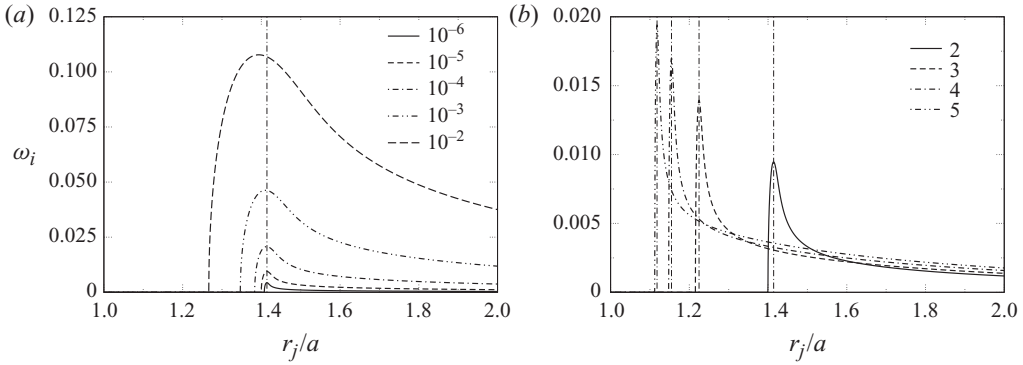


FIGURE 3. Growth rate for a heavy-cored Rankine vortex as a function of density jump location. (a) For various Atwood numbers, as shown in the legend, for  $m = 2$ .  $At$  increases upwards in powers of 10 starting from  $10^{-2}$ . (b) At fixed  $At = 10^{-5}$ , for various  $m$ , as shown in the legend. In both plots, the dash-dot vertical lines indicate the critical radius obtained from (3.11).

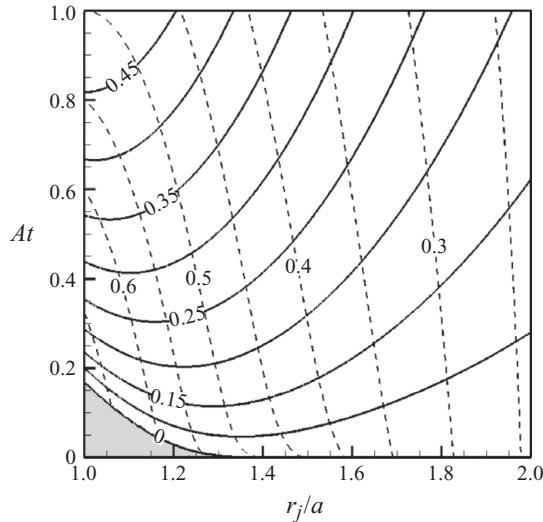


FIGURE 4. Contours of growth rate in the  $At$ - $r_j/a$  plane for heavy-cored vortex ( $At > 0$ ). Only the region outside the core is indicated, since a density jump within the core would be stable. Solid lines indicate growth rate, and dashed lines the frequency. Grey shading represents neutral regions.

When  $m = 2$ , this condition is met when  $At > 0.171$ , and for  $m = 3$ , when  $At > 0.101$ . A physical explanation for the stabilization will become apparent after the discussion in §3.3.

### 3.2. Light-cored Rankine vortex

If unstable density stratification can be stabilized, then the natural question that arises is whether the reverse is also true, i.e. can a light-cored vortex flow ever be unstable. To put the present results in perspective, it is re-emphasized that the earlier work of Sipp *et al.* (2005) and Joly *et al.* (2005) did not find any destabilization for any density contrast using Gaussian profiles. In this subsection, we see that a Rankine core with a step density jump can be unstable. In the next section, we show that instability occurs only for steep profiles.

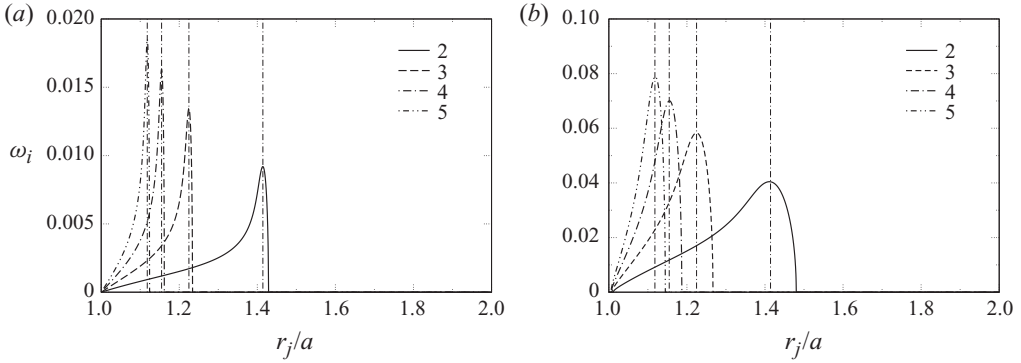


FIGURE 5. (a) Variation of growth rate with the jump location for a light-cored Rankine vortex at (a)  $At = -10^{-5}$ , (b)  $At = -10^{-3}$ . The dash-dot vertical line indicates  $r_c$ .

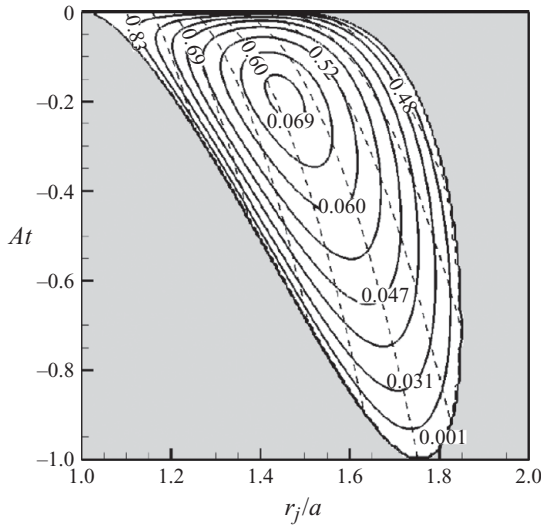


FIGURE 6. Contours of growth rate in the  $At-r_j$  plane for a light-cored vortex ( $At < 0$ ). Solid lines indicate growth rate and dashed lines indicate frequency. The grey shading represents a neutral region.

For a light-cored vortex,  $At < 0$ . At low ( $-At$ ), instability now occurs when  $\mathcal{P}$  in (3.12) is less than 0. From (3.11), it is again seen that instability first occurs at the critical radius as the Atwood number is increased (negatively) from zero. Instability is now confined to the region immediately outside the core as shown in figure 5. The complete dispersion relation for a light-cored vortex with  $m = 2$  is plotted in figure 6.

The three solutions of (3.6), named  $\omega^{(1)}$ ,  $\omega^{(2)}$  and  $\omega^{(3)}$  may be obtained from series expansions in Atwood number. We derive an outer solution denoted by a superscript  $o$ , valid away from the critical radius and an inner solution, denoted by a superscript  $i$ , valid in the neighbourhood of the critical radius. The first solution, corresponding to the Kelvin wave riding on the vortex core boundary in the homogeneous case, takes the asymptotic form

$$\omega^{(1),o} = \omega_0^{(1),o} + (-At) \omega_1^{(1),o} + O(-At)^2, \tag{3.15}$$

where

$$\omega_0^{(1),o} = \frac{m-1}{2} \quad \text{and} \quad \omega_1^{(1),o} = \frac{(m-1) \left(\frac{a}{r_j}\right)^{2m} \left[ (m-1) - 2m \left(\frac{a}{r_j}\right)^{2m} + m \left(\frac{a}{r_j}\right)^4 \right]}{2(m-1)^4 - 4m(m-1) \left(\frac{a}{r_j}\right)^2 + 2m^2 \left(\frac{a}{r_j}\right)^4}. \tag{3.16}$$

This solution diverges at the critical radius  $r_c$ , but since it gives rise to no instability, that neighborhood is not studied in detail. The other two solutions, which describe the continuous spectrum modes localized at  $r = r_j$ , take the asymptotic form

$$\omega^{(2,3),o} = \omega_0^{(2,3),o} + (-At)^{1/2} \omega_1^{(2,3),o} + O(-At), \tag{3.17}$$

with

$$\left. \begin{aligned} \omega_0^{(2,3),o} &= \frac{ma^2}{2r_j^2}, \\ \omega_1^{(2,3),o} &= \pm \left[ \frac{-3 \left(\frac{a}{r_j}\right)^{2m+4} (2m^2 + m) - 3m(m-1) \left(\frac{a}{r_j}\right)^4 + 4m^2 \left(\frac{a}{r_j}\right)^6}{12 \left( m \left(\frac{a}{r_j}\right)^2 - (m-1) \right)} \right]^{1/2}. \end{aligned} \right\} \tag{3.18}$$

These solutions too diverge at the critical radius. An inner solution in this neighborhood takes the asymptotic form

$$\omega^{(2,3),i} = \omega_0^{(2,3),i} + (-At)^{1/3} \omega_1^{(2,3),i} + O(-At)^{2/3}, \tag{3.19}$$

where the correction term  $\omega_1^{(2,3),i}$  is obtained as a solution to the equation

$$\begin{aligned} \omega_1^2 &\left( \frac{m \left(\frac{a}{r_j}\right)^2}{2} - \frac{m-1}{2} + (-At)^{1/3} \omega_1 \right) \\ &= (-At)^{1/3} \frac{m}{8} \left(\frac{a}{r_j}\right)^4 \left( m \left(\frac{a}{r_j}\right)^2 - (m-1) - \left(\frac{a}{r_j}\right)^{2m} \right). \end{aligned} \tag{3.20}$$

Thus, a continuous spectrum mode localized at  $r = r_j$  becomes unstable with a growth rate increasing as  $|At|^{1/2}$  when  $r_j \gg r_c$ . In a small region around the critical radius of the Kelvin wave, the growth rate increases faster, as  $|At|^{1/3}$ .

### 3.3. Physical mechanism

In §§3.1 and 3.2, we showed that a light-cored ( $At < 0$ ) Rankine vortex can be destabilized. We now examine the physical mechanism behind this process. A corresponding explanation may be offered for the stabilization of a heavy-cored vortex. The mechanism, of wave interaction, relies on the existence of two differentially moving free waves (these are neutral waves having an independent existence and are associated with perturbation vorticity localized in space), which can slow each other down relatively until they settle into a normal mode, see, e.g. Hoskins *et al.* (1985). The final phase difference between the two will determine the production of perturbation energy, and therefore decide whether the combined system will be stable. This can

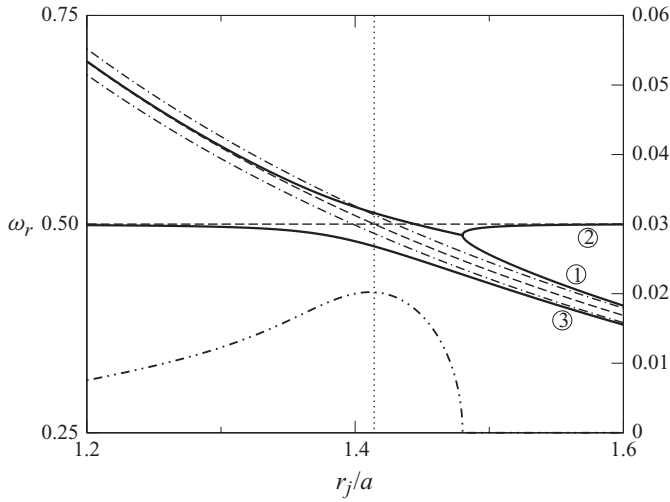


FIGURE 7. Variation of frequencies (solid lines) with radial location of the density jump of the three solutions for light cored Rankine vortex with  $m = 2$  and  $At = -10^{-3}$ . The growth rate of the unstable mode is shown by the dash-dot-dot line. The dashed curves correspond to (3.10) for a Rankine vortex at  $At = 0$ . The dash-dot curves indicate the frequencies for a point-vortex system derived from (2.16). The vertical dotted line shows  $r_c$ .

be seen both by performing an energy balance, or as done below, by a simple mechanistic argument. In our flow, the interaction is between internal waves at the density interface and a Kelvin wave on the Rankine vortex.

The solid lines in figure 7 show the three eigenvalue branches of perturbations on a Rankine vortex as functions of  $r_j$ , where the step density jump is placed. The growth rates corresponding to the unstable mode are shown by the dash-dot-dot lines. The branches contain the effects of both the vorticity step at the edge of the Rankine vortex, and the density step at  $r_j$ . In order to understand the origin of each branch, we plot separately the solutions to (i) a Rankine vortex in a homogeneous density fluid, and (ii) a circular density interface around a point vortex. The former are obtained from (3.10), and are shown by the dashed lines in the figure. The dispersion relation for the latter may be derived from (2.16), and for a typical Atwood number, lie on either side of the homogeneous  $\omega^{2,3}$ , as shown by the dash-dot curves. Starting at large  $r_j$  in the figure and proceeding leftwards, we see that branch 1, corresponding to the faster moving density wave, interacts with the Kelvin mode, branch 2. At an  $r_j$  not far from the critical value, they combine to give eigenvalues thereafter which form a complex conjugate pair.

Using the eigenfunctions given in Appendix A, interface displacements and perturbation vorticity may be seen to take the forms

$$\eta_a = \frac{ia^{-m-1}}{\left[ \left(\frac{r_j}{a}\right)^{2m} (\omega - (m-1)\Omega_0) - \Omega_0 \right]}, \tag{3.21a}$$

$$\eta_j = \frac{ir^{-m-1}}{\omega - m\Omega \frac{a^2}{r_j^2}}, \tag{3.21b}$$

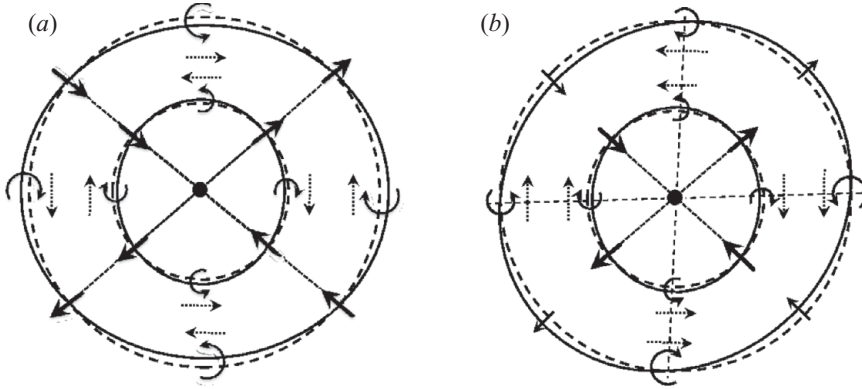


FIGURE 8. Wave interaction for a light-cored Rankine vortex. The perturbed interfaces at  $r = a$  and  $r = r_j$  are shown by the solid line. Dashed lines indicate the unperturbed location. The straight solid arrows indicate the induced velocity at the nodes of the interfaces and dashed arrows indicate the direction of the tangential velocity disturbance. The circular arrows denote the disturbance vorticity. (a) Neutral configuration. The radial velocity perturbation  $u_r$  does not affect the density interface. (b) Unstable configuration, where  $u_r$  destabilizes the outer sheet.

$$\zeta_a = \frac{2i\Omega_0 a^{-m-1}}{\left[ \left(\frac{r_j}{a}\right)^{2m} (\omega - (m-1)\Omega_0) - \Omega_0 \right]} \delta(r-a), \tag{3.22a}$$

$$\zeta_j = \frac{-2ir_j^{-m-1} \left[ \left(\frac{r_j}{a}\right)^{2m} (\omega - (m-1)\Omega_0) \right]}{\left[ \left(\frac{r_j}{a}\right)^{2m} (\omega - (m-1)\Omega_0) - \Omega_0 \right]} \delta(r-r_j), \tag{3.22b}$$

where  $\eta$  and  $\zeta$  are the amplitudes of the perturbed interface location and the perturbation vorticity, respectively, and the subscripts refer to radial locations  $a$  and  $r_j$ . The phases between various quantities on the twin vortex sheets may be derived from the above, and are shown schematically in figure 8. Figure 8(a) corresponds to  $r_j \gg r_c$ , where all modes are neutrally stable, while shown in figure 8(b) is the situation at an  $r_j \sim r_c$ , where the instability growth rate is the maximum. The difference we would like to highlight is the phase between the two interfaces in each figure, and the phase between the density interface and the radial velocity perturbation. In the neutrally stable situation, the two interfaces are in phase, and both are perfectly out of phase with the radial velocity. Thus,  $u_r$  neither abets nor impedes the interface displacement. If one rotates the Kelvin wave, being the faster moving, in the anti-clockwise direction, it can be worked out that the outer vortex sheet will respond so as to return the system to the original phase. On the other hand, for a growing mode, we need the interfaces to be positioned such that  $\eta_j$  lags  $\eta_a$  to within half a wavelength. In the most dangerous case,  $\eta_a$  and  $\eta_j$  are out of phase, and  $u_r$  causes  $\eta_j$  to grow. The Kelvin mode thus acts as a source of energy, absent in the point vortex case. This is the essential mechanism for the instability of a light-cored vortex. In other words, for a neutral wave, the kinematic condition  $D\eta/Dt = u_r$  means that the interface displacement and the normal velocity are always out of phase, i.e. there is no production of disturbance energy. Once the waves interact, and  $\eta$  and  $u_r$  are

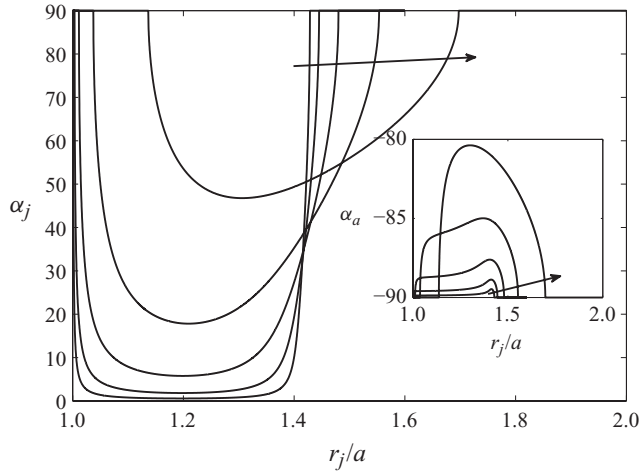


FIGURE 9. Phase difference,  $\alpha_j$  and  $\alpha_a$ , between interface displacement and radial velocity at  $r=r_j$  and  $r=r_a$ , respectively. The Atwood number for the curves increases from  $10^{-5}$  to  $10^{-1}$  in powers of 10 as indicated by the arrow. For  $m=2$ , an angle of  $90^\circ$  represents a half-wavelength displacement in the azimuthal direction.

locked at a particular phase, an instability can result. To see where such interaction happens, an approximate estimate of the phase is obtained by putting  $\omega_1 \approx m\Omega_0 a^2/r_j^2$  in (3.21). We may see that for  $r_j \gtrsim r_c$ , the two interfaces are in phase, whereas below  $r_c$ , the interfaces are no longer in phase.

Figure 9 shows the variation of the phase angle  $\alpha$  between  $\eta$  and  $u_r$  at both interfaces as a function of  $r_j$ . Since  $m=2$  here, a half-wavelength displacement in the azimuthal direction is represented by an angle of  $90^\circ$ . For the smallest  $At$  considered, the two interfaces behave like free waves and this results in near-perfect phase locking between the density interface and the radial velocity below the critical radius. The phase angle at  $r=a$  shown in the inset departs marginally from the neutral wave condition, i.e.  $\alpha_a \approx -90^\circ$ . This too indicates that it is the density interface that is destabilized, rather than the vortex core. The above discussion can be easily extended to explain the stabilization of a heavy-cored vortex.

The kinematic picture described above is in agreement with the wave energetic viewpoint of linear wave interactions. The wave energy concepts first developed in plasma physics were introduced into hydrodynamics by Cairns (1979). A detailed discussion of wave energetics is given in Craik (1985) and Fabrikant & Stepanyants (1998). The wave energy can be calculated from the dispersion relation using the formula

$$\mathcal{E} = \frac{1}{4} \omega \frac{\partial D}{\partial \omega} |\eta_0|^2, \quad (3.23)$$

where  $\mathcal{E}$  is the wave energy,  $D$  is the cubic dispersion relation of (3.6) multiplied by a negative sign and  $\eta_0$  is the interface displacement amplitude. Instability occurs when the dispersion curves of two waves with oppositely signed wave energies intersect. This happens in the present case, since branch 1 can be shown to be associated with positive wave energy, while the Kelvin mode, as Fukumoto (2003) showed, is associated with a negative wave energy.

#### 4. Stability of smooth profiles

Given that a light-cored Rankine vortex with step density jump can be unstable, but a light-cored Gaussian vortex with a Gaussian density distribution is not (Joly *et al.* 2005), it is clear that the smoothness of the profile has a crucial role to play. In §4.1, we demonstrate that for smooth profiles too, instabilities similar to that for a Rankine vortex can exist, if the variation in the mean flow is rapid enough. With increasing smoothness however, the corresponding growth rates decrease and, at some smoothness, instabilities vanish. How may this be explained, i.e. what happens to the mathematical construct of free waves we created above, when the discontinuities, as in real life, are smoothed out?

As shown by Briggs *et al.* (1970) and is now well known, smooth vorticity profiles do not have discrete normal mode solutions. However, a subset of the continuous spectrum, lying in the vicinity of the critical radius of a related sharp profile, can take the place of the discrete mode. In other words, the collaboration of these continuous spectrum modes (which actually appear as singular wave packet solutions) can lead to remarkably wave-like behaviour. When this happens, it is referred to as a quasi-mode ((Briggs *et al.* 1970); (Schecter *et al.* 2000) and others). These quasi-modes exhibit an exponential decay, much in the manner of a stable discrete wave, for a short time. At longer times, we have the usual algebraic decay (Case 1960) of the entire continuous spectrum. The exponential decay can often be associated with the least stable Landau pole. Landau poles are discrete eigenvalues of the inviscid (Rayleigh) stability equation, obtained from an analytic continuation into the complex plane. Since they exist in another Riemann surface, they have to be distinguished from true eigenmodes. It is well known now that when vorticity gradient at the critical radius is very small, then Landau poles indeed become quasi-modes, i.e. manifest wave-like behaviour in the physical Riemann surface. On physical grounds, the exponential damping has been interpreted as being due to a resonant wave–fluid interaction, analogous to the wave–particle interaction considered by Landau. Schecter *et al.* (2000) showed that this resonant damping is a result of the conservation of angular momentum, where phase mixing of vorticity in the Kelvin’s cat’s eye at the critical layer leads to a decrease in the mode amplitude. The existence of quasi-modes can be ascertained by various qualitative measures as we shall see.

As the base vorticity becomes more spread out, its resemblance to a step vorticity change becomes weaker, and so does the connection between the displayed behaviour and the Landau pole. Consequently, the behaviour will be seen to be no longer wave-like at high levels of smoothness. In particular, as Schecter *et al.* (2000) noted, a Gaussian vortex has no noticeable quasi-mode signature. In this case, an initial impulsive perturbation results in a spiral structure which does not resemble a normal mode. Secondly, the pole lies so far from the real  $r$  line that a critical radius is not well-defined. Since the deviation from wave-like behaviour is gradual with increase in smoothness, a particular smoothness level at which a quasi-mode ceases to exist is not possible to define in this flow.

By various measures, we show that a profile less smooth than about  $n = 4$  exhibits quasi-mode behaviour. More important, we show that quasi-modes possess another property of wave-like disturbances, in that like discrete waves, they can participate in interactions with other waves. Interestingly, the interaction in this case between an exponentially decaying quasi-mode of the vortex profile and a neutral internal wave results in exponential growth. This interaction can also be interpreted in terms of wave energies. Briggs *et al.* (1970) showed that quasi-modes possess negative wave energy. Hence, the mode amplitude grows when energy is extracted from these waves,

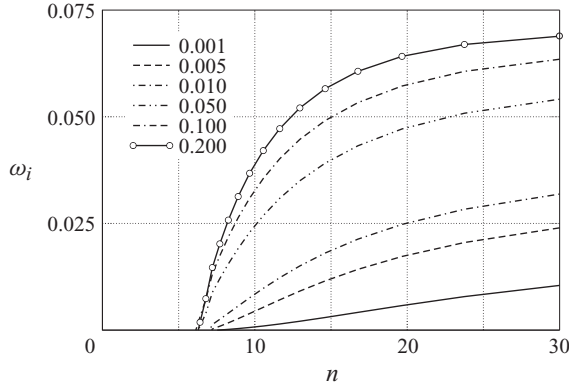


FIGURE 10. Growth rates obtained by varying the value of  $n$  for vortex and density profiles for different Atwood numbers. The density profiles are placed at  $r_c$ .

by either introducing friction (viscosity) in the system, or by introducing a positive energy wave. The former situation occurred in Briggs *et al.* (1970), while we let ourselves into the latter situation by introducing positive energy waves due to density stratification.

#### 4.1. Quasi mode – gravity wave interaction

We now present stability results on the family of smooth vorticity profiles described earlier. Equation (2.16) is solved in the domain  $r=0$  to  $R_{\max}$ , which is fixed at 20, using the Chebyshev spectral collocation method. A change in the domain size to 15 or 30 did not change the eigenvalues significantly. Convergence checks were carried out for most of our results. The collocation points are defined in the domain  $x \in [-1, 1]$  which is then mapped on to a radial coordinate. The grid is clustered in radial regions of sharp density gradients based on the stretching formula given in Govindarajan (2004). To improve accuracy at small growth rates and to obtain Landau poles, the integration contour is deformed into a plane of complex radius  $r^*$ . All the above are incorporated in the following:

$$r^* = \beta_1 \left[ \frac{\sinh(\beta_2((1+x)/2 - y_0)) + \sinh(\beta_2 y_0)}{\sinh(\beta_2 y_0)} \right] - i\alpha(1 - x^2), \tag{4.1}$$

where

$$y_0 = \frac{1}{2\beta_2} \log \left[ \frac{1 + (e^{\beta_1} - 1)\beta_1}{1 + (e^{-\beta_1} - 1)\beta_1} \right]. \tag{4.2}$$

Here,  $\beta_1$  represents the location where clustering is desired,  $\beta_2$  determines the degree of clustering, and  $\alpha < 0$  denotes the extent of deformation. For radially stratified vortices, we choose  $\beta_1$  to coincide with the density jump location. For homogenous flows treated later in the paper,  $\beta_1$  is chosen to be equal to the critical radius.  $\beta_2$  is fixed at 10 in all our calculations. It was seen above that instability for a Rankine vortex is highest when the density jump is placed at the critical radius. To get an estimate of the maximum growth rate, we again place the density jump at the critical radius, defined now as the real part of the Landau pole location of the homogeneous vortex, as described in detail later. In figure 10, growth rates for different Atwood numbers are shown as functions of profile steepness. For the Atwood numbers considered here, instability always vanishes for  $n$  less than about 6. On the other hand, for large

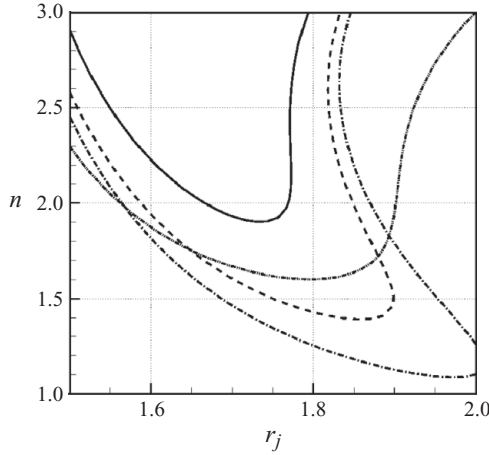


FIGURE 11. Neutral curves with tanh density profiles (2.7) of  $\delta_t = 0.1$ . solid line:  $At = -0.01$ , dashed line:  $At = -0.02$ , dash-dot line:  $At = -0.025$ . Dash-dot-dot line:  $At = -0.05$  with the density profile according to (2.5) with  $n = 10$ .

$n$ , the Rankine limit is approached. The density profiles here have the same  $n$  as the vorticity. To estimate how much of the stabilization at lower  $n$  is due to the smoothing of the density profiles, a steep tanh density profile, as given in (2.7), is used to obtain neutral stability curves, shown in the  $n - r_j$  plane in figure 11. The steepening of the density profile does bring down the  $n$  at which instabilities vanish. Though its exact value is sensitive to  $At$ , for small  $At$ , this  $n$  value is always between 2 and 1. Henceforth, we use only steep density profiles.

In the small  $At$  limit, waves from vortex and density profiles can be assumed to weakly modify each other. For large  $At$ , vorticity and density waves strongly influence each other, making it difficult to pin down a particular range of  $n$  for the transition to stability.

In the next subsection, we study the stability properties of a homogeneous vortex. The  $At$  is set to zero in the rest of this section.

#### 4.2. Landau poles and quasi-modes for a homogeneous vortex

To estimate how wave-like the vorticity perturbation is, we prescribe homogeneous density conditions in this subsection. Landau poles are recovered from a suitable analytic continuation of the dispersion relation, as discussed in Briggs *et al.* (1970). We then qualitatively estimate whether these are also quasi-modes of the system.

Figure 12 shows the frequency and decay rate as per the Landau pole as functions of the smoothness parameter  $n$ . For large  $n$ , the frequency approaches asymptotically the Kelvin mode frequency of a Rankine vortex. The decay rate increases dramatically for  $n \lesssim 3.5$ . Eventually, at low enough  $n$ , we have  $\omega_{q,i}/\omega_{q,r} \sim O(1)$ , violating the assumption of small decay rate of Briggs *et al.* (1970) and Schecter *et al.* (2000), under which they are able to obtain quasi-modes. An examination of figure 13 reveals that the critical point  $r_c$  too drifts rapidly away from the real- $r$  axis for  $n \lesssim 3.5$ , so the approximation of the critical point by its projection on the real axis is not justified. We therefore expect that there should be no quasi-mode evident at low  $n$ , and apply some diagnostics to support this.

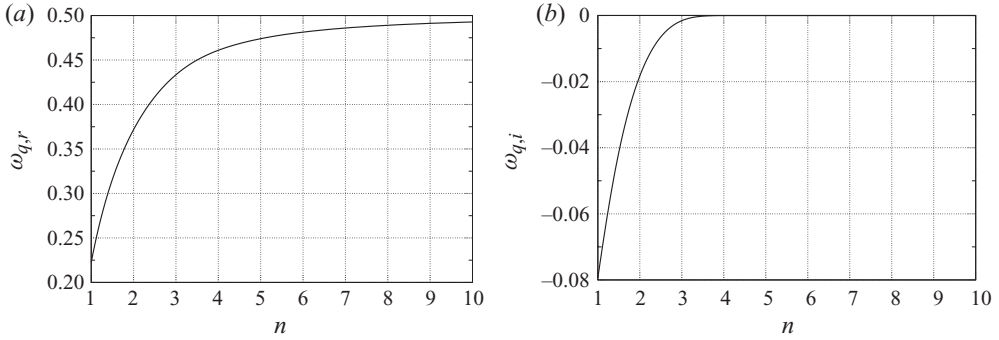


FIGURE 12. Variation of Landau pole  $\omega_q$  for  $m=2$ . Subscripts r and i indicate the real and imaginary parts.  $\omega_{q,i}$  has a negative value for all  $n$ , but is too small to be visible when  $n > 3.5$ . A sudden drop in  $\omega_{q,r}$  is obtained for  $n \lesssim 3.5$ .

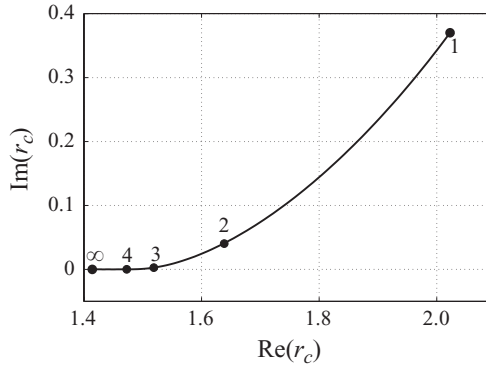


FIGURE 13. Location of the Landau pole in the complex  $r$ -plane for various values of  $n$  with  $m=2$ . The limiting values for a Rankine vortex ( $n \rightarrow \infty$ ) with critical radius at  $\sqrt{2}$  and a Gaussian vortex ( $n=1$ ) along with a few intermediate values of  $n$  are indicated by bold circles. A large increase in  $\text{Im}(r_c)$  is obtained for  $n \lesssim 3.5$ .

The first is the excitability test of Schecter *et al.* (2000). The excitability, which they define as

$$X_l = - \frac{\langle \xi_l, r^{m-1} \mathcal{D}Z(r) \rangle}{\langle \xi_l, \xi_l \rangle}, \tag{4.3}$$

is a measure of amplification of a given frequency in the perturbation. Here, the inner product is defined as

$$\langle f, g \rangle = \int_0^\infty \frac{f^*(r)g(r)}{|\mathcal{D}Z(r)|} r^2 dr, \tag{4.4}$$

and the disturbance vorticity is considered in discretized form, for example in terms of Chebyshev polynomials, as

$$\zeta(r, t) = \sum_{l=1}^N a_l \xi_l(r) e^{-i\omega_l t}, \tag{4.5}$$

where  $a_l$  are the expansion coefficients,  $\xi_l$  the vorticity eigenfunction and  $\omega_l$  is the frequency. In the case of steep tanh vortices, Schecter *et al.* (2000) obtained a Lorentzian-type excitability spectrum, with a peak at the Landau frequency. This is

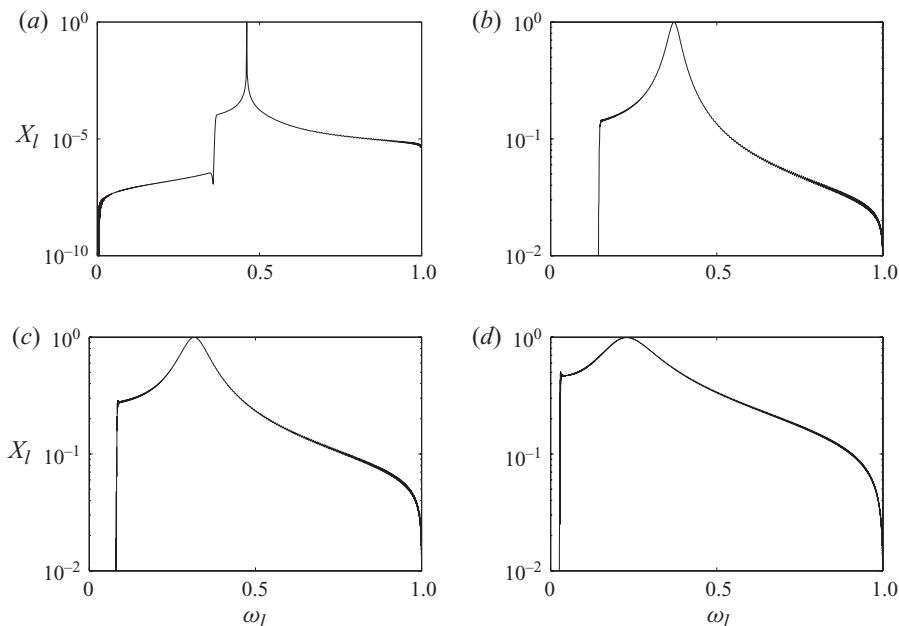


FIGURE 14. Excitability for vorticity profiles with (a)  $n = 4$ , (b)  $n = 2$ , (c)  $n = 1.5$  and (d)  $n = 1$ . Note the change of vertical scale for (a). A sharply peaked excitability spectrum is indicative of a quasi-mode.

the signature of a quasi-mode. However, for a Gaussian vortex, a broadband spectrum was obtained with no well-defined peak. Our results for the present profiles are in qualitative agreement, as seen in the excitability spectra in figure 14 for four vorticity profiles of decreasing steepness. Given its sharply peaked excitability spectrum, we estimate that a profile of  $n = 4$  is steep enough to respond with a wave, and at some lower  $n$ , a quasi-mode no longer exists. In fact, the excitability spectrum for  $n = 4$  is fit well by a Lorentzian, with a peak at  $\text{Re}(\omega_q)$ , where the subscript  $q$  stands for the Landau pole, that is orders of magnitude greater than for surrounding frequencies. For  $n = 2$  and 1.5, there is only a shallow peak, while a Gaussian vortex behaves in accordance with Schecter *et al.* (2000).

Fabre, Sipp & Jacquin (2006), whose primary focus was 3D perturbations, provided a second diagnostic. They too noted that a Gaussian vortex does not have a quasi-mode in the 2D limit, displaying instead a broadband response. Their viscous L-branches (as they name them), the only modes which can possess a critical layer singularity, undergo a dramatic change in eigenmode structure as axial wavenumber is decreased (see their figure 14). For small axial wavenumber and large Reynolds number, the disturbance is wound into a thin spiral structure outside the vortex core, notably with no perturbation in the core region. If a resonant wave–fluid interaction were taking place, we would have seen its signature in the form of a significant perturbation amplitude at the core. They further showed that these viscous L-branch solutions at large  $Re$  match the inviscid solutions of Sipp & Jacquin (2003) suggesting that the quasi-modes of the inviscid system become true eigenmodes of the viscous problem. Moreover, decay rates of these L-branch solutions rapidly increases with decreasing axial wavenumber, such that eventually  $\omega_{q,i} \sim O(\omega_{q,r})$ . This led Fabre *et al.* (2006) to conclude that there are no quasi-modes for a Gaussian vortex in the 2D

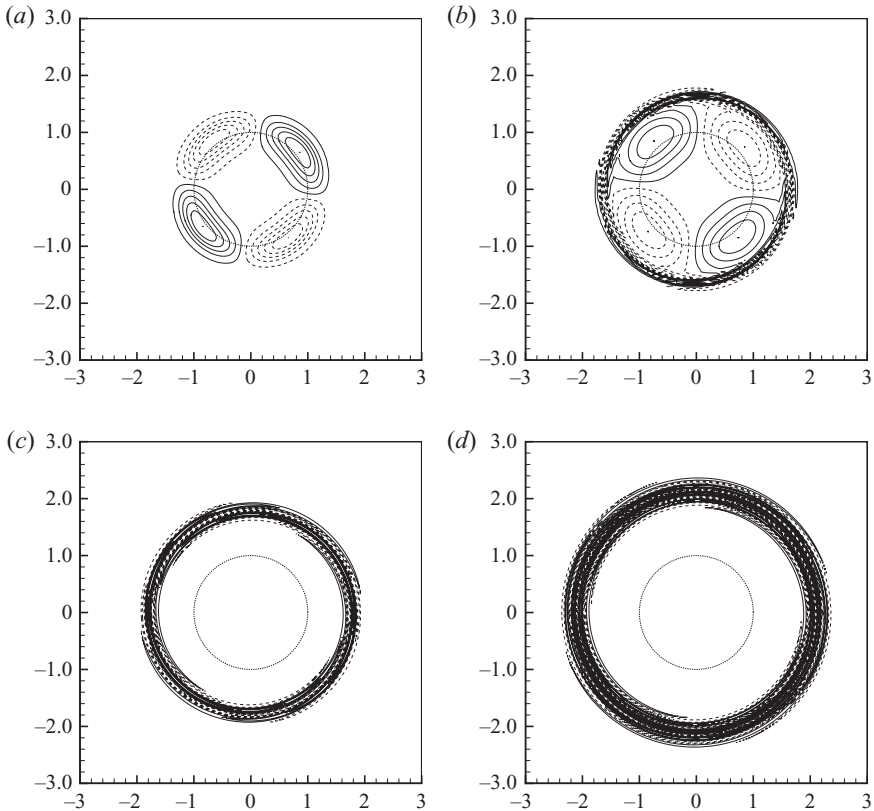


FIGURE 15. Vorticity eigenfunctions for homogeneous vortices obtained from a viscous calculation at  $Re = 10^5$ . (a)  $n = 4$ , (b)  $n = 2$ , (c)  $n = 1.5$  and (d)  $n = 1$ . The dotted circle at the centre indicates the vortex core size  $\delta_z$ . Twelve equally spaced contour levels are plotted. Solid and dashed lines indicate positive and negative vorticity levels, respectively.

limit. We extend the viscous stability study to other values of  $n$ , with the governing equations and method described in Dixit & Govindarajan (2010). The results at  $Re = 10^5$  shown in figure 15 indicate that there are significant vorticity perturbations inside the core for  $n \geq 2$ , suggesting again that quasi-modes exist for steeper profiles.

#### 4.3. Initial value problem

In the solution of an initial value problem, quasi-modes are associated with exponential decay of energy, where the decay rate is precisely that given by the Landau pole. This provides a third diagnostic. The linear equations (2.9)–(2.12) are solved with homogeneous boundary conditions at  $r = 0$  and  $r = R_{max}$ . Radial discretization is given by (4.1) with  $\alpha = 0$  and we use 3000 collocation points. The initial perturbation consists of a narrow ring of vorticity centered at the real part of the critical radius  $\text{Re}(r_c)$ , with

$$\zeta(r, 0) = \exp\left(\frac{-(r - \text{Re}[r_c])^2}{\delta^2}\right). \quad (4.6)$$

A large number of vorticity profiles were studied, but we present only a few. We are specifically interested in the region between  $n = 4$  and  $n = 1$ . One way to measure

$n$	$\omega_q$	$r_c$
3.5	$0.450 - 1.856 \times 10^{-4}i$	$1.490 + 0.307 \times 10^{-3}i$
3.0	$0.433 - 1.518 \times 10^{-3}i$	$1.518 + 0.266 \times 10^{-2}i$
2.47	$0.407 - 6.892 \times 10^{-3}i$	$1.567 + 0.133 \times 10^{-1}i$
2.0	$0.371 - 1.827 \times 10^{-2}i$	$1.638 + 0.406 \times 10^{-1}i$
1.5	$0.315 - 4.137 \times 10^{-2}i$	$1.766 + 0.118i$
1.0	$0.222 - 7.939 \times 10^{-2}i$	$2.022 + 0.370i$

TABLE 1. Variation of Landau pole for select values of profile smoothness. The critical location for these modes lies off the real axis, and is obtained by inverting the relation  $\omega_q = m\Omega(r_c)$ .

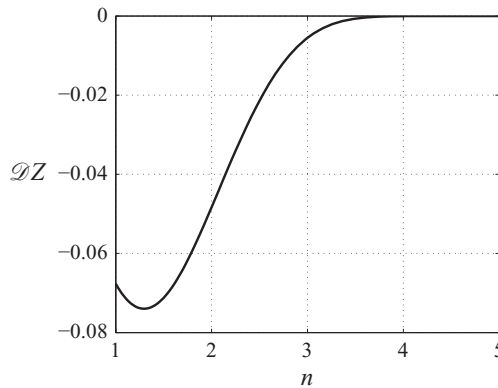


FIGURE 16. Vorticity gradient at the critical radius for various values of  $n$ . The solid line is the real part of  $\mathcal{D}Z$  obtained by considering the complex  $r_c$  and the dotted line is obtained by calculating  $\mathcal{D}Z$  at  $r = \text{Re}(r_c)$ . The minima in these two cases are reached at  $n = 1.3$  and  $n = 1.6$ , respectively.

the strength of non-axisymmetric perturbations is to use the  $m$ th multipole moment defined as

$$Q_m(t) = \int_0^\infty r^{m+1} \zeta(r, t) \, dr. \tag{4.7}$$

This quantity is a measure of the ellipticity of the vortex (for  $m = 2$ ) and is related to the form of the streamfunction in the far-field, i.e.

$$Q_m(t) \sim 2mr^m \psi_m(t), \quad (r \rightarrow \infty), \tag{4.8}$$

(see Bassom & Gilbert (1998); Turner & Gilbert (2007)). For comparison, table 1 gives Landau pole values and their critical radii for a few vortex profiles. As seen in figure 17, the decay rate obtained from the multipole moment,  $Q_m(t)$ , is in excellent agreement with table 1 for profiles  $n = 2$  and  $n = 1.5$ , but the agreement is not so good for  $n = 1$ . The exponential decay is seen to last for longer times as the profile is made steeper. The noise at late times is probably due to insufficient numerical resolution, since the disturbance field becomes progressively finer-scaled. A very small viscosity has been used to stabilize some of the calculations (as done by (Turner & Gilbert 2007)).

Another useful quantity is the kinetic energy of the perturbations, defined as

$$E(t) = \int_0^\infty \frac{r}{m^2} (m^2 \|u_r\|^2 + \|\mathcal{D}(ru_r)\|^2) \, dr. \tag{4.9}$$

$n$	$\text{Im}(\omega_q)$	$\sigma_q$	$\sigma_e$
2.0	-0.01827	-0.01827	-0.01827
1.5	-0.04137	-0.04137	-0.0325
1.0	-0.07939	-0.054	-0.0245

TABLE 2. Comparison of decay rate obtained from multipole moment and energy with the Landau pole value for three different vortex profiles. The decay rate of energy for  $n=2$  vortex is in excellent agreement with the Landau pole value, but is poor for the other profiles.

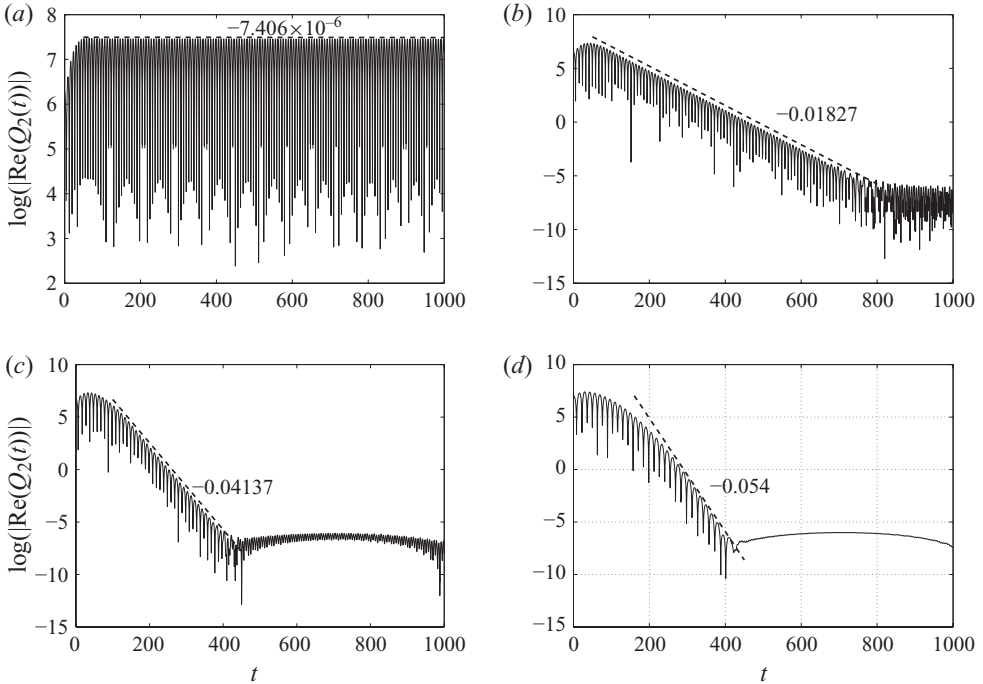


FIGURE 17. Evolution of quadrupole moment  $|\text{Re}(Q_2(t))|$  for four different vortex profiles, (a)  $n=4$ , (b)  $n=2$ , (c)  $n=1.5$  and (d)  $n=1$ . The dashed lines are fits for the exponential damping rate with the indicated decay rate.

At intermediate times, larger than the mean turnover time,  $E(t)$  being proportional to  $\exp(-2\omega_{q,i}t)$  is a definitive demonstration of quasi-mode response. Figure 18 shows the evolution of normalized kinetic energy. After a short early transient, a clear exponential decay can be noticed, similar to the observations of Shrira & Sazonov (2001) in a boundary layer flow. A striking distinction between the decay of  $Q_m(t)$  and  $E(t)$  is the significantly shorter duration of exponential decay in  $E(t)$ . Decay rates  $\sigma_q$  and  $2\sigma_e$ , obtained by a fit of the exponential portions of  $Q_m(t)$  and  $E(t)$ , respectively, are tabulated in table 2. Again, the decay of  $Q_m(t)$  is in fair comparison with the Landau pole value, but the decay of energy is in poor agreement for  $n=1.5$  and  $n=1$  vortices. The transient growth is seen in the inset of figure 18 to increase with increasing  $n$  at short times. But the exponential decay rate at intermediate times does not change monotonically with  $n$ ; at  $n=1.5$ , the decay is more rapid than at

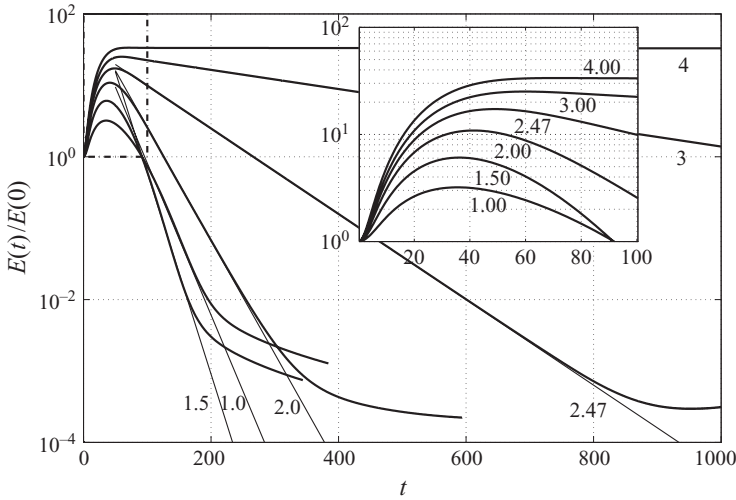


FIGURE 18. Evolution of disturbance kinetic energy  $E(t)$  in homogeneous vortices for  $n=1, 1.5, 2, 2.47, 3$  and  $4$  indicated by solid lines. An exponential fit of the form  $e^{2\sigma t}$  is obtained and is shown for the first four curves. Values of  $\sigma$  obtained for  $n=1, 1.5, 2$  and  $2.47$  are  $-0.0245, -0.0325, -0.01827$  and  $-0.006892$ , respectively. The inset shows the region near  $t=0$  indicated by a rectangle, where transient growth is obtained. Notice a monotonic increase in transient energy growth with  $n$ , but a non-monotonic variation in energy decay.

$n=1$  or  $n=2$ . The decay rate is expected to be directly related to  $\mathcal{D}Z(r_c)$ , and a corresponding non-monotonicity in that quantity is seen in figure 16.

To compare the response of the initial value problem with the viscous stability calculations, a fixed time of 100, close to the beginning of the energy decay, is chosen. Figure 19 shows the contours of perturbation vorticity at  $t=100$  for four different values of  $n$ . Figures 19(a), 19(b) and 19(c) are remarkably similar to the viscous results shown in figure 15, suggesting that quasi-modes indeed become eigenmodes of the viscous problem. Clearly, a lobed structure analogous to a Kelvin wave can be noticed at  $r=a$  (shown by a dotted circle) for the  $n=4$  vortex. For an  $n=2$  vortex, weak lobes are noticed at the core boundary. Core perturbations completely vanish for an  $n=1.5$  vortex, and in the case of  $n=1$ , the spiral region begins to engulf the vortex core with no visible wave-like pattern noticeable.

Having seen by all measures that no quasi-mode exists for  $n < 1.5$ , we now examine the light-cored vortex. Clearly from figure 11, the instability vanishes for  $n$  between 2 and 1. We thus conclude that the existence of a quasi-mode is strongly correlated with the existence of an instability. We surmise that the quasi-mode makes a wave interaction possible.

### 5. Nonlinear stages

We now present results from a viscous direct numerical simulation to understand the nonlinear stages of these instabilities. Even in stably stratified shear flows like the Holmboe instability, there continues to be interest in understanding these instabilities in the nonlinear regime (see the recent paper of (Carpenter *et al.* 2010)). In the light of this interest in a parallel flow, it would be of interest to understand similar situations for a rotating flow. Only the results for light-cored vortices are presented, as the heavy-cored case has already been treated in Joly *et al.* (2005) and Coquart

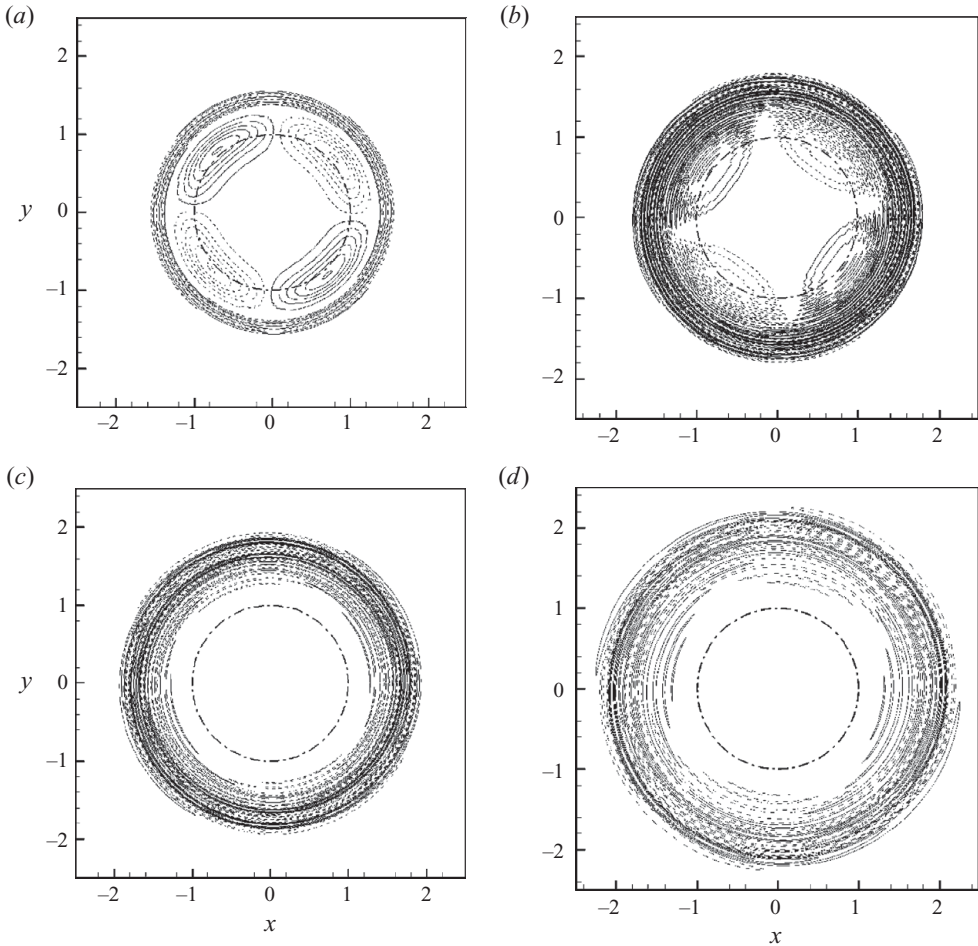


FIGURE 19. Contours of perturbation vorticity for a homogeneous vortex obtained from a linear initial value problem at  $t = 100$ . (a)  $n = 4$ , (b)  $n = 2$ , (c)  $n = 1.5$  and (d)  $n = 1$ . Twenty equally spaced contour levels between the maximum and minimum values are plotted. The positive levels are shown by solid lines and negative levels by dashed lines. The dotted circle shows the region of the vortex core. Note the change of scale for (d).

*et al.* (2005). In many flows, the nonlinear pattern bears strong similarities with the most unstable mode obtained from a linear analysis. Heavy-cored vortices were shown by Joly *et al.* (2005) to split into  $m$  smaller but stronger vortices. But with stable stratification in light-cored vortices, it is interesting to know what would be the outcome of an exponentially growing instability. We find initial adherence to the linear growth rate followed by nonlinear saturation. However, unlike in the heavy-cored case where the primary vortex splits into  $m$  parts, baroclinically generated vorticity creates  $m$  additional satellite vortices around the primary vortex, forming a stable nonlinear structure. For an  $m = 2$  perturbation, the saturated state takes the form of a tripolar vortex. This is the first study to our knowledge which shows that a tripolar vortex can be created from a vortex profile in the presence of a 'stable' density stratification. Incidentally, in an experimental realization of an unstratified tripolar vortex, van Heijst & Kloosterziel (1989) and van Heijst, Kloosterziel & Williams (1991) use an initial negative vorticity envelope. This envelope makes the vortex susceptible

to barotropic instabilities. Carton, Flierl & Polvani (1989) exploit these unstable modes to obtain stable tripolar vortices in their numerical simulations at constant density.

### 5.1. Numerical method and initial perturbation

The numerical method is a 2/3-dealized pseudo-spectral code Canuto *et al.* (1988) solved in the vorticity-streamfunction formulation with periodic boundary conditions for an incompressible non-Boussinesq fluid. This enforces a solenoidal velocity field. An additional equation is solved for the non-axisymmetric correction to the density field. The characteristic scales in the problem, as given in section (2.1), are determined by the vortex core size,  $\delta_z$ , density core size,  $\delta_\rho$  and circulation  $\mathcal{E}$ . For simplicity, we consider the transport coefficients to be constant. To enable comparison with the stability analysis presented in §4, we consider a large Reynolds number,  $Re$  and Peclet number,  $Pe$  in the present simulations. This allows us to approach inviscid results with viscosity and diffusivity to stabilize the numerical scheme. The governing equations solved in cartesian coordinates can be written as

$$\frac{d\tilde{Z}}{dt} = \frac{1}{\tilde{\rho}} \left( \frac{\partial \tilde{\rho}}{\partial y} \frac{d\tilde{u}}{dt} - \frac{\partial \tilde{\rho}}{\partial x} \frac{d\tilde{v}}{dt} \right) + \frac{1}{Re} \nabla^2 \tilde{Z}, \quad (5.1)$$

$$\frac{d\tilde{\rho}}{dt} = \frac{1}{Pe} \nabla^2 \tilde{\rho}. \quad (5.2)$$

Here  $d/dt$  represents the total derivative, and  $\tilde{Z}$  and  $\tilde{\rho}$  are the total vorticity and density fields. The first term on the right-hand-side of (5.1) is responsible for baroclinic torque created by a misalignment of pressure and density surfaces. These are the standard equations for an incompressible fluid where density varies across the flow (see e.g. (Birman, Martin & Meiburg 2005) and (Dixit & Govindarajan 2010)). We use a unit Schmidt number, so  $Re = Pe = \mathcal{E}/\nu$ . A large value of 50 000 was chosen. A domain size of  $L = 8\pi$  in  $x$  and  $y$  directions was chosen and we use  $1024^2$  grid for all the cases. Periodicity enforces a net zero circulation in the flow, and hence the velocity field far away from the vortex axis is not accurately predicted. This prompts us to use a large domain size. This was found to be very important in order to capture the transient periods of the instability.

At  $t=0$ , an initial perturbation is given to the vorticity and density fields

$$\tilde{Z}(r, \theta, t) = Z(r) + \epsilon \hat{Z}(r, \theta, t), \quad (5.3)$$

$$\tilde{\rho}(r, \theta, t) = \rho(r) + \epsilon \hat{\rho}(r, \theta, t). \quad (5.4)$$

Here,  $[Z(r), \rho(r)]$  are the base state vorticity and density profiles as defined in §2,  $[\hat{Z}(r, \theta), \hat{\rho}(r, \theta)]$  are perturbation vorticity and density fields normalized by  $\max[\hat{Z}(r, \theta)]$ , and  $\epsilon$  controls the initial amplitude of the perturbation, to be discussed later. We fix the profile parameter  $n$  at 10 for both vorticity and density, as we did not wish to carry out a detailed parametric study for the present work. Other values of  $n$  are expected to give qualitatively similar results. This choice of  $n$  was found to be ideal for the present problem as it provided a sufficiently large growth rate for a wide range of Atwood numbers which could be easily captured in the numerical simulations, and at the same time, the profile was sufficiently smooth to describe the steep gradients well while using a smaller number of total grid points. A larger value of  $n$  would require a much finer grid than used here.

Run	$n$	$At$	$m$	$\delta_\rho/\delta_z$	$\omega_r(\text{lin})$	$\omega_i(\text{lin})$
1	10	-0.2	2	1.5	0.5803	0.04606
2	10	-0.5	2	1.5	0.6520	0.04377
3	10	-0.2	3	1.5	0.9874	0.02826
4	10	-0.5	3	1.5	1.0370	0.05190

TABLE 3. Description of the various parameters used in the numerical simulations.  $\omega_r(\text{lin})$  and  $\omega_i(\text{lin})$  are the frequencies and growth rates obtained from a linear stability analysis.

An inviscid stability analysis was first carried out with an  $n=10$  vorticity and density profile to obtain discrete (unstable) eigenmodes. For simplicity, we fix the ratio of vortex and density core sizes at a value of 1.5. A viscous stability analysis at  $Re = Pe = 50000$  did not produce any appreciable difference in the results. The numerical simulations carried out are listed in table 3, but only a few representative results are presented. In figure 20, initial perturbations for vorticity and density fields are plotted for runs 1 and 3. The perturbations are organized as  $2m$  spiral arms, and an additional rim of vorticity at the density interface can be noticed. This additional outer rim of vorticity is crucial to the formation of stable nonlinear structures.

These perturbations are now added to base state vorticity and density, and a small value of  $\epsilon$ , fixed at 0.01, is used. Computations were also carried out with  $\epsilon = 0.05, 0.1$ . No appreciable difference was noticed in the results, but a shorter linear regime was obtained. With a value of  $\epsilon = 0.01$ , the peak vorticity perturbation value was  $1/100$  of the base state vorticity value at the vortex axis, and the peak density perturbation value was approximately  $1/600$  of the average density value. These are small enough for linear dynamics to be captured well.

## 5.2. Results

In figures 21 and 22, we plot the full nonlinear time evolution of vorticity and density fields for run 1, which corresponds to an  $m=2$  perturbation with  $At = -0.2$ . At initial time, negative vorticity levels are about two orders of magnitude smaller than the maximum vorticity level. Time in these plots is non-dimensionalized by maximum vorticity value. After a very early transient adjustment of the perturbation field, an exponential growth ensues, whose rate is in good agreement with linear stability prediction. At  $t=40$ , a ring of negative vorticity is formed around the vortex. This ring soon organizes itself into two satellite vortices. By  $t=80$ , a fully developed tripolar vortex is formed, and at  $t \approx 100$ , saturation of  $|Q_2(t)|$  is observed. To quantify the eccentricity of the perturbation field, we numerically calculate the multipole moment for  $m=2$ . This is plotted in figure 23. Upon saturation, a flat region which survives for many turnover time periods may be seen. The evolution of the square of the density fluctuations averaged over the simulation domain is plotted in figure 24(a). In our simulations, we directly calculate the non-axisymmetric part of the density field,  $\hat{\rho}(x, y, t)$ , and from this we obtain

$$\langle \hat{\rho}(t)^2 \rangle = \int_0^L \int_0^L \hat{\rho}(x, y, t) dx dy. \quad (5.5)$$

We additionally place monitor points across the density interface along a given radial line, and instantaneous values of total density were extracted at each time step. The time evolution of instantaneous density at five such monitor points is shown in figure 24(b). The first and last monitor points are far away from the density interface,

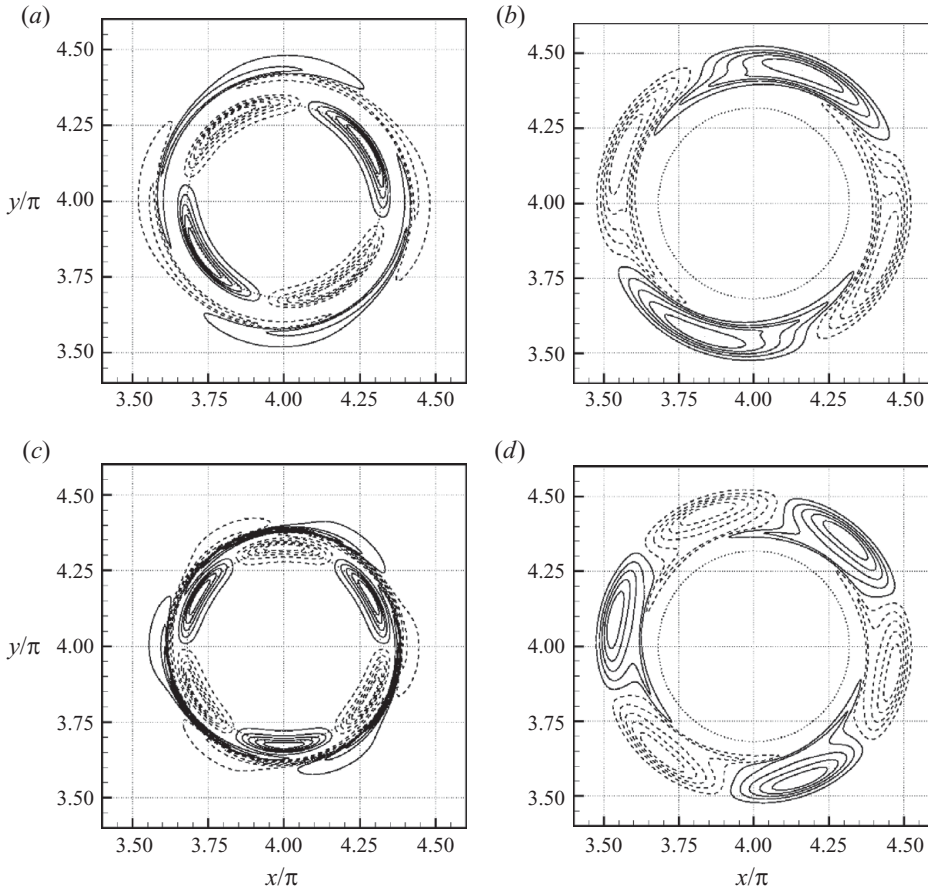


FIGURE 20. Vorticity (*a,c*) and density (*b,d*) perturbation corresponding to the most unstable eigenmode for an  $n=10$  vortex from a linear stability calculation. This is the initial condition for the simulations.  $At=-0.2$  and  $m=2$  for the first row, and  $At=-0.5$  and  $m=3$  for the second row. Twelve equally spaced contours between maximum and minimum values plotted.

and are placed inside and outside the density core, respectively. At these two points, there is no change in density value up to an error of  $10^{-6}$ , whereas at other points, an oscillatory signal is obtained. The frequency spectrum yielded a dominant frequency of 0.57, which is in excellent agreement with the linear stability calculations. In fact, this rotation rate is seen to vary very little even for a fully developed tripolar vortex.

Because of the finite value of viscosity, vorticity in these satellites slowly homogenizes. At  $t=200$ , the vorticity in the satellites is still an order of magnitude smaller than in the primary vortex. The whole structure slowly advects relative to the flow. Density contour plots in figure 22 offer a good visualization of the flow field. The reversal of vorticity field in the satellites is clearly accompanied by density contours being twisted in the clock-wise direction. The final tripolar vortex formed is observed to be stable for a very long period of time, and is only weakened slightly due to viscosity. Nonetheless,  $Re=50\,000$  was observed to be a large enough value for inviscid dynamics to be captured. Smaller Reynolds number simulations were also carried out, and they yielded similar results.

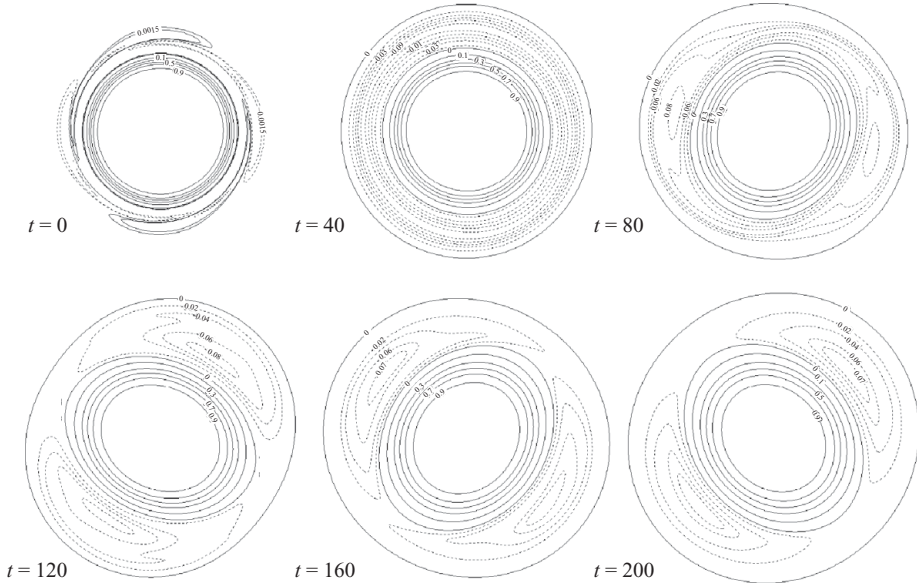


FIGURE 21. Vorticity contours at various times for Run-1 with  $m=2$  and  $At=-0.2$ . Notice the smallness of negative vorticity levels indicated with dashed lines. All figures are to the same scale as shown in figure 20. The nonlinear saturation into a tripolar state of an initially stably stratified configuration is evident.

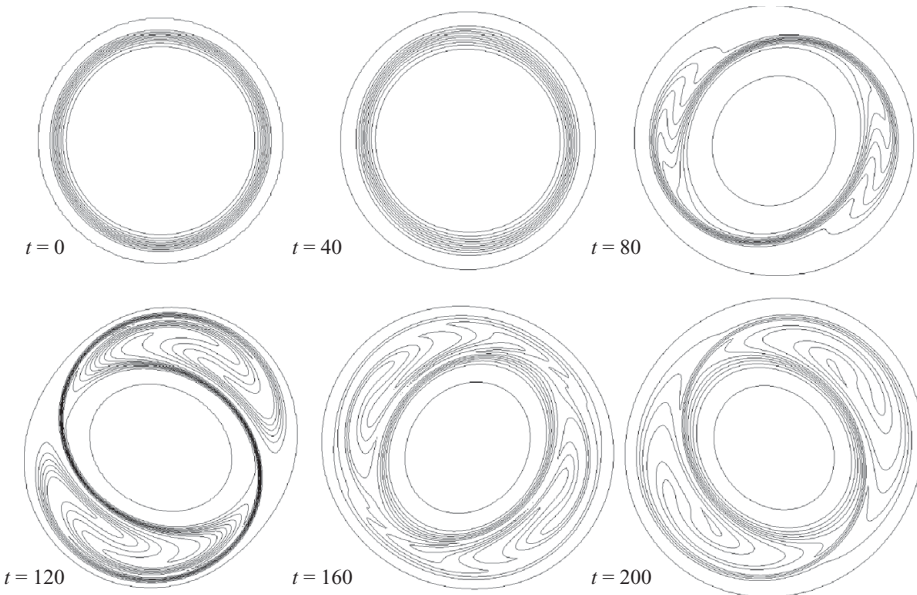


FIGURE 22. Density contours at various times for Run-1 with  $m=2$  and  $At=-0.2$ . Twelve equally spaced contour levels between  $\max(\bar{\rho})$  and  $\min(\bar{\rho})$  are shown.

## 6. Summary and discussion

The problem of a vortex in a density stratification has been studied many times before. The studies found the expected result, namely that a light-cored vortex is always stable, and a heavy-cored one usually unstable. We show here situations

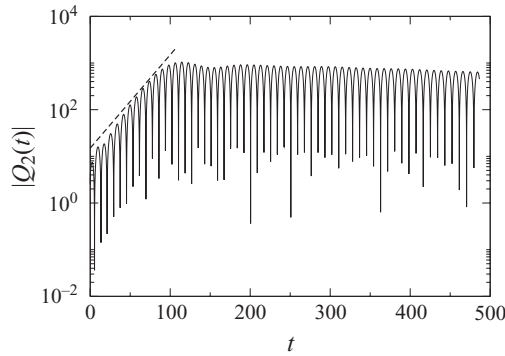


FIGURE 23. Multipole moment for Run-1 with  $m = 2$  and  $At = -0.2$ . The dashed line indicates prediction from linear stability calculation and has a slope of 0.04606, as shown in table 3. The best fit for the numerical slope is approximately 0.051, in good agreement with the linear stability result. The flattening of  $|Q_2(t)|$  at  $t > 100$  corresponds to nonlinear saturation into a tripolar vortex.

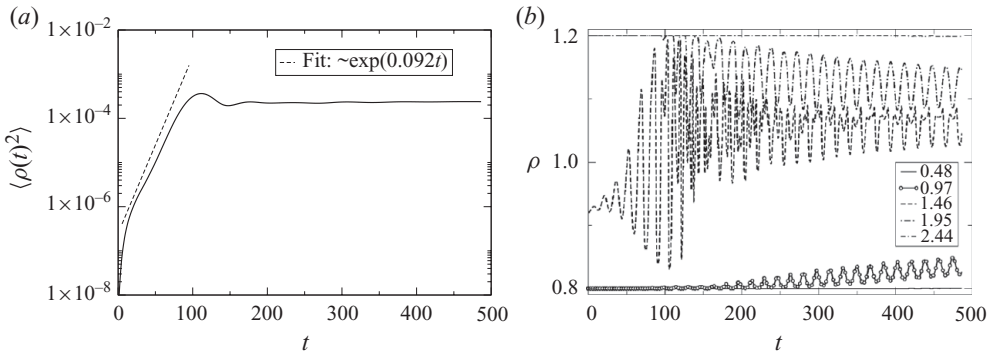


FIGURE 24. (a) Time evolution of  $\rho(t)^2$  averaged over the entire domain, i.e.  $\langle \rho(t)^2 \rangle$  for Run-1 simulation with  $m = 2$  and  $At = -0.2$ . (b) Time trace for the same case showing evolution of instantaneous density extracted from various monitor points placed along a radial line at radii 0.48, 0.97, 1.46, 1.95 and 2.44. A fast Fourier transform (FFT) spectrum yields a dominant frequency of 0.57, in excellent agreement with linear stability calculation shown in table 3.

where, remarkably, the opposite happens, with a light-cored vortex going unstable, and a heavy-cored one stabilizing. Though the latter situation has found mention earlier, the reason was not clarified. We show that there are two requirements for the unexpected behaviour. (i) the variation in vorticity and density must be confined to thin layers, and (ii) these two layers of rapid variation must lie relatively close to each other. For a Rankine vortex, the best location for the density interface is in the vicinity of the critical layer of the Kelvin mode. The reason that earlier work, in particular that of Joly *et al.* (2005), did not find this counter-intuitive result is that they used a Gaussian vortex, not one with a steeply-varying vorticity. In addition, in a Gaussian vortex, regions of shear and vorticity overlap. This makes it harder to discern the role of shear in the stabilization of a heavy-cored vortex. By studying a class of profiles of varying smoothness, we derive a level of steepness below which no instability is seen. Further, we show that for small Atwood numbers, instability growth rates of light-cored vortices are comparable to their heavy-cored counterparts.

It is seen that shear is necessary for the interaction, so a density jump placed within a region of solid-body rotation would be uninteresting. An expansion for small Atwood numbers shows that the growth rate of the instability scales as  $|At|^{1/3}$  in the vicinity of the critical layer, and only as  $|At|^{1/2}$  closer to the vortex core. Thus, the instability appears first at  $r_c$  and is strongest in that vicinity. When  $r_j$  increases away from  $r_c$ , there is a steep fall-off in the instability. Conversely, in a heavy-cored vortex, a jump placed in the region immediately outside the core, but within  $r_c$ , is stabilized. An Atwood number criterion for instability when the vorticity and density jumps coincide is derived. The physical mechanism leading to the destabilization of a light-cored Rankine vortex is explained as two neutral waves interacting to give exponential growth. Further support for the mechanism is given by wave-energetic arguments.

For smooth but steep profiles, the instability is described as being caused by the interaction between the quasi-mode of the homogeneous vortex and an internal wave arising due to density inhomogeneity. A direct mathematical proof of this result was found to be too difficult at this stage, but this work demonstrates the feasibility of such an interaction within the linear regime. Due to a non-zero vorticity gradient at the critical radius, all smooth vortex profiles possess Landau poles with an exponentially decaying solution. In the steep ( $n \rightarrow \infty$ ) limit, we show that these Landau poles indeed become discrete neutral eigenmodes of the Rankine vortex, but for small  $n$ , the exponential decay rate in an initial value problem departs from the Landau pole prediction. The eigenfunction structure in this case is dominated by a spiral outside the core with no vorticity inside it (also see (Schechter *et al.* 2000) and (Fabre *et al.* 2006)).

Quasi-modes have earlier been studied in the context of nonlinear resonant triad interactions. Here, we show that they might be useful to interpret linear instabilities in smooth profiles. In particular, we have shown that a quasi-mode can behave exactly like a wave in its interaction with another wave.

In a stratified turbulent flow, we expect this new mechanism to be displayed in terms of multipolar vortices arising from a single light-cored vortex. This is because we expect a nonlinear saturation, especially given the overall stabilizing influence of density. Our direct numerical simulations confirm this, giving stable tripolar and quadrupolar vortices corresponding to  $m=2$  and 3 perturbations. The numerically obtained exponential growth of perturbations at short times compares well with the linear stability predictions.

An extension of the present work to 3D flows would be interesting in many ways. Stratification can be considered both in the axial direction as has been recently studied by Le Dizès (2008) and Le Dizès & Billant (2009), and in the radial direction as done here. With constant axial stratification, internal gravity waves can radiate away from the vortex, leading to radiative instabilities. Moreover, the fact that a 3D Rankine vortex supports an infinite number of discrete Kelvin modes tremendously increases the possibilities of wave interactions. Some progress in this direction has been made.

The authors thank A. Roy for suggesting many useful references and discussions, especially regarding the relevance of quasi-modes. Figure 8 was inspired by schematics of G. Subramanian.

## Appendix A. Derivation of Rankine vortex dispersion relation

In the three regions for a Rankine vortex with a density jump given by (3.5), the general solutions of (2.16) take the form,  $r^{m-1}$  and  $r^{-m-1}$ . The complete solution can

be written as

$$u_r = \begin{cases} A_1 r^{m-1}, & \text{if } r < a, \\ A_2 r^{m-1} + A_3 r^{-m-1}, & \text{if } a < r < r_j, \\ r^{-m-1}, & \text{if } r > r_j. \end{cases} \quad (\text{A } 1)$$

The constants  $A_1$ ,  $A_2$  and  $A_3$  can be found by matching radial velocity at  $r = a$  and  $r = r_j$  and pressure across  $r = a$ , and this gives

$$A_1 = \frac{(\omega - m\Omega_0)a^{-2m}}{\left[ \left( \frac{r_j}{a} \right)^{2m} (\omega - (m-1)\Omega_0) - \Omega_0 \right]}, \quad (\text{A } 2)$$

$$A_2 = \frac{(\omega - (m-1)\Omega_0)a^{-2m}}{\left[ \left( \frac{r_j}{a} \right)^{2m} (\omega - (m-1)\Omega_0) - \Omega_0 \right]}, \quad (\text{A } 3)$$

$$A_3 = \frac{-\Omega_0}{\left[ \left( \frac{r_j}{a} \right)^{2m} (\omega - (m-1)\Omega_0) - \Omega_0 \right]}. \quad (\text{A } 4)$$

Finally, matching pressure across the density jump gives us (3.6), a cubic dispersion relation in the eigenvalue  $\omega$ . From the continuity equation, the azimuthal velocity perturbation can be written as

$$u_\theta = \frac{ir}{m} \mathcal{D}^* u_r. \quad (\text{A } 5)$$

The form of  $u_r$  on either side of the two interfaces shows that there exists a jump in  $u_\theta$  at  $r = a$  and  $r = r_j$ , i.e. there is a vortex sheet at each of the two interfaces. The vortex sheet strength is given by

$$\Delta u_\theta|_{r=a} = \frac{2i\Omega_0 a^{-m-1}}{\left[ \left( \frac{r_j}{a} \right)^{2m} (\omega - (m-1)\Omega_0) - \Omega_0 \right]}, \quad (\text{A } 6)$$

$$\Delta u_\theta|_{r=r_j} = -2ir_j^{-m-1} \frac{\left[ \left( \frac{r_j}{a} \right)^{2m} (\omega - (m-1)\Omega_0) \right]}{\left[ \left( \frac{r_j}{a} \right)^{2m} (\omega - (m-1)\Omega_0) - \Omega_0 \right]}. \quad (\text{A } 7)$$

#### REFERENCES

- ABRAMOWITZ, M. & STEGUN, I. A. (Ed.) 1972 *Handbook of Mathematical Functions with Formulas, Graphs, and Mathematical Tables*. Dover.
- BAINES, P. G. & MITSUDERA, H. 1994 On the mechanism of shear flow instabilities. *J. Fluid Mech.* **276**, 327–342.
- BASSOM, A. P. & GILBERT, A. D. 1998 The spiral wind-up of vorticity in an inviscid planar vortex. *J. Fluid Mech.* **371**, 109–140.
- BIRMAN, V. K., MARTIN, J. E. & MEIBURG, E. 2005 The non-Boussinesq lock-exchange problem. Part 2. High-resolution simulations. *J. Fluid Mech.* **537**, 125–144.
- BRIGGS, R. J., DAUGHERTY, J. D. & LEVY, R. H. 1970 Role of Landau damping in crossed-field electron beams and inviscid shear flow. *Phys. Fluids* **13** (2), 421–432.

- CAIRNS, R. A. 1979 The role of negative energy waves in some instabilities of parallel flows. *J. Fluid Mech.* **92**, 1–14.
- CANUTO, C., HUSSAINI, M. Y., QUARTERONI, A. & ZANG, T. A. 1988 *Spectral Methods in Fluid Dynamics*. Springer.
- CARPENTER, J. R., TEDFORD, E. W., RAHMANI, M. & LAWRENCE, G. A. 2010 Holmboe wave fields in simulation and experiment. *J. Fluid Mech.* **648**, 205–223.
- CARTON, X. J., FLIERL, G. R. & POLVANI, L. M. 1989 The generation of tripoles from unstable axisymmetric isolated vortex structures. *Europhys. Lett.* **9**, 339–344.
- CASE, K. M. 1960 Stability of an inviscid plane Couette flow. *Phys. Fluids* **3**, 143–148.
- COQUART, L., SIPP, D. & JACQUIN, L. 2005 Mixing induced by Rayleigh–Taylor instability in a vortex. *Phys. Fluids* **17**, 021703.
- CRAIK, A. D. D. 1985 *Wave Interactions and Fluid Flow*. Cambridge University Press.
- DIXIT, H. N. & GOVINDARAJAN, R. 2010 Vortex-induced instabilities and accelerated collapse due to inertial effects of density stratification. *J. Fluid Mech.* **646**, 415–439.
- DRAZIN, P. G. & REID, W. H. 1981 *Hydrodynamic Stability*. Cambridge University Press.
- ECKHOFF, K. S. & STORESLETTEN, L. 1978 A note on the stability of steady inviscid helical gas flows. *J. Fluid Mech.* **89**, 401–411.
- ECKHOFF, K. S. & STORESLETTEN, L. 1980 On the stability of rotating compressible and inviscid fluids. *J. Fluid Mech.* **99**, 433–448.
- FABRE, D., SIPP, D. & JACQUIN, L. 2006 Kelvin waves and the singular modes of the Lamb–Oseen vortex. *J. Fluid Mech.* **551**, 235–274.
- FABRIKANT, A. L. & STEPANYANTS, YU. A. 1998 *Propagation of Waves in Shear Flows*. World Scientific Series on Nonlinear Science.
- FUKUMOTO, Y. 2003 The three-dimensional instability of a strained vortex tube revisited. *J. Fluid Mech.* **493**, 287–318.
- FUNG, Y. T. 1983 Non-axisymmetric instability of a rotating layer of fluid. *J. Fluid Mech.* **127**, 83–90.
- FUNG, Y. T. & KURZWEIG, U. H. 1975 Stability of swirling flows with radius-dependent density. *J. Fluid Mech.* **72**, 243–255.
- GANS, R. F. 1975 On the stability of a shear flow in a rotating gas. *J. Fluid Mech.* **68**, 403–412.
- GOVINDARAJAN, R. 2004 Effect of miscibility on the linear stability of a two-fluid channel. *Intl. J. Multiphase Flow* **30**, 1177–1192.
- HALL, I. M., BASSOM, A. P. & GILBERT, A. D. 2003 The effect of fine structure on the stability of planar vortices. *Eur. J. Mech. (B/Fluids)* **22**, 179–198.
- HARNIK, N., HEIFETZ, E., UMURHAN, O. M. & LOTT, F. 2008 A buoyancy–vorticity wave interaction approach to stratified shear flow. *J. Atmos. Sci.* **65**, 2615–2630.
- VAN HEIJST, G. J. F. & KLOOSTERZIEL, R. C. 1989 Tripolar vortices in a rotating fluid. *Nature* **338**, 569–571.
- VAN HEIJST, G. J. F., KLOOSTERZIEL, R. C. & WILLIAMS, C. W. M. 1991 Laboratory experiments on the tripolar vortex in a rotating fluid. *J. Fluid Mech.* **225**, 301–331.
- HOSKINS, B. J., MCINTYRE, M. E. & ROBERTSON, A. W. 1985 On the use and significance of isentropic potential vorticity maps. *Q. J. R. Meteorol. Soc.* **111**, 877–946.
- HOWARD, L. N. 1961 Note on a paper of John W. Miles. *J. Fluid Mech.* **10**, 509–512.
- HOWARD, L. N. & MASLOWE, S. A. 1973 Stability of stratified shear flows. *Boundary-Layer Meteorol.* **4**, 511–523.
- JOLY, L., FONTANE, J. & CHASSAING, P. 2005 The Rayleigh–Taylor instability of two-dimensional high-density vortices. *J. Fluid Mech.* **537**, 415–431.
- KOCHAR, G. T. & JAIN, R. K. 1979 Note on Howard’s semicircle theorem. *J. Fluid Mech.* **91**, 489–491.
- KURZWEIG, U. H. 1969 A criteria for the stability of heterogenous swirling flows. *Z. Angew. Math. Phys.* **20**, 141–143.
- LE DIZÈS, S. 2008 Inviscid waves on a Lamb–Oseen vortex in a rotating stratified fluid: consequences for the elliptic instability. *J. Fluid Mech.* **597**, 283–303.
- LE DIZÈS, S. & BILLANT, P. 2009 Radiative instability in stratified vortices. *Phys. Fluids* **21**, 096602 (1–8).
- LEES, L. 1958 Note on the stabilizing effect of centrifugal forces on the laminar boundary layer over convex surfaces. *J. Aero. Sci.* **25**, 407–408.

- MCWILLIAMS, J. C., GRAVES, L. P. & MONTGOMERY, M. T. 2003 A formal theory for vortex Rossby waves and vortex evolution. *Geophys. Astrophys. Fluid Dyn.* **97**, 275–309.
- NADIGA, B. T. & AURNOU, J. M. 2008 A tabletop demonstration of atmospheric dynamics: Baroclinic instability. *Oceanography* **21**, 196–201.
- PRESS, W. H., TEUKOLSKY, S. A., VETTERLING, W. T. & FLANNERY, B. P. 1992 *Numerical Recipes in C: The Art of Scientific Computing*. Cambridge University Press.
- ROMANOVA, N. N. 2008 Resonant interaction of waves of continuous and discrete spectra in the simplest model of a stratified shear flow. *Izvestiya, Atmospheric and Oceanic Physics* **44**, 53–63.
- ROMANOVA, N. N. & SHRIRA, V. I. 1988 Explosive generation of surface waves by wind. *Izv. Atmos. Ocean. Phys.* **24**, 528–535.
- SAKAI, S. 1989 Rossby–Kelvin instability: a new type of ageostrophic instability caused by a resonance between Rossby waves and gravity waves. *J. Fluid Mech.* **202**, 149–176.
- SAUNDERS, P. M. 1973 The instability of a baroclinic vortex. *J. Phys. Oceanogr.* **3**, 61–65.
- SAZONOV, I. A. 1989 Interaction of continuous-spectrum waves with each other and with discrete-spectrum waves. *Fluid Dyn. (translated from Izv. Akad. Nauk SSSR)* **24**, 586–592.
- SCHECTER, D. A., DUBIN, D. H. E., CASS, A. C., DRISCOLL, C. F., LANSKY, I. M. & O'NEIL, T. M. 2000 Inviscid damping of asymmetries on a two-dimensional vortex. *Phys. Fluids* **12**, 2397–2412.
- SCHECTER, D. A. & MONTGOMERY, M. T. 2003 On the symmetrization rate of an intense geophysical vortex. *Dyn. Atmos. Oceans* **37**, 55–88.
- SHRIRA, V. I. & SAZONOV, I. A. 2001 Quasi-modes in boundary-layer-type-flows. Part 1. Inviscid two-dimensional spatially harmonic perturbations. *J. Fluid Mech.* **446**, 133–171.
- SIPP, D., FABRE, D., MICHELIN, S. & JACQUIN, L. 2005 Stability of a vortex with a heavy core. *J. Fluid Mech.* **526**, 67–76.
- SIPP, D. & JACQUIN, L. 2003 Widnall instabilities in vortex pairs. *Phys. Fluids* **15**, 1861–1874.
- TAYLOR, G. I. 1931 Effect of variation in density on the stability of superposed streams of fluid. *Proc. R. Soc. Lond. A.* **132**, 499–523.
- TURNER, M. R. & GILBERT, A. D. 2007 Linear and nonlinear decay of cat's eyes in two-dimensional vortices, and the link to Landau poles. *J. Fluid Mech.* **593**, 255–279.
- UBEROI, M. S., CHOW, C. Y. & NARAIN, J. P. 1972 Stability of coaxial rotating jet and vortex of different densities. *Phys. Fluids* **15**, 1718–1727.
- VALLIS, G. K. 2006 *Atmospheric and Oceanic Fluid Dynamics*. Cambridge University Press.
- VANNESTE, J. 1996 Rossby wave interaction in a shear flow with critical levels. *J. Fluid Mech.* **323**, 317–338.
- VORONOVICH, A. G. & RYBAK, S. A. 1978 Explosive instability of stratified currents. *Dokl. Acad. Sci. USSR* **239**, 1457–1460.
- VORONOVICH, V. V., PELINOVSKY, D. E. & SHRIRA, V. I. 1998a On the internal waves shear flow resonance in shallow water. *J. Fluid Mech.* **354**, 209–237.
- VORONOVICH, V. V., SHRIRA, V. I. & STEPANYANTS, YU. A. 1998b Two-dimensional modes for nonlinear vorticity waves in shear flows. *Stud. Appl. Maths* **100**, 1–32.